Heat Transfer-Friction Factor and Correlations for Wavy Porous Screens as Inserts in Channel Thermal Performance

A. Torr

Mechanical and Aeronautical Engineering Department, University of Pretoria, South Africa.

andrewt@resonant.co.za

G.I. Mahmood*

Mechanical and Aeronautical Engineering Department, University of Pretoria, South Africa.

gazi.mahmood@up.ac.za

*Corresponding author

L. Cramer

Mechanical and Aeronautical Engineering Department, University of Pretoria, South Africa.

lcramer@illovo.co.za

Abstract

Structural inserts are employed to enhance the heat transfer in channel flow with the expense of thermal performance. The present investigation employs the wavy porous screens as inserts in an air channel and measures the pressure drop and heat transfer along the channel. The wave vectors are parallel to the flow and in point contact at the tips with the channel walls. The pores in the insert generate turbulence to enhance the heat transfer from the channel walls with moderate pressure penalty because of the low blockage ratio. The objectives are to investigate the effects of wavelength (λ), porosity (ξ), and height (H) of the sinusoid wave of the insert as well as the Reynolds number on the friction factors and Nusselt numbers. Twelve inserts are formed from the flat metal mesh screens for testing between the Reynolds number (Re) of 400 and 35000. The results of (f, Nu) and smooth channel based enhancements (f/f_0, Nu/Nu_0) are affected the most by the Re followed by the λ and then ξ. The values of both (f/f_0, Nu/Nu_0) increase significantly as the Reynolds number increases in $Re <$ 3000. However, both the (f/f_0, Nu/Nu_0) decrease little as both the (λ, ξ) increase at all Re. The

performance factor index, $(Nu/Nu_0)/(f/f_0)^{(1/3)} > 1.0$ irrespective of (λ, ξ, H) only when the Re is about 3000. The correlations developed for the f, Nu, and performance factor provide reasonable predictions of the experimental results.

Keywords: Friction factor, Nusselt number, Thermal performance, Porosity, Wave length.

1. Introduction

Wavy thin plates are commonly used as internal fins in channel heat transfer enhancement in flat plate heat exchangers, electronic cooling channels, solar absorbers, motor casings etc. The fin plates also provide structural supports to the channel walls as the wave vectors are oriented along the mean flow direction and wave tips are permanently bonded to the channel walls [1, 2]. Some of the plates use structured holes to reduce the pressure penalty in the channel flow. The present study employs wavy porous screens as inserts made of interwoven thin metal-wires to replace the wavy thin plates in the channels and measures the convective heat transfer and pressure penalty along the channels. The screen also supports the channel walls as the wave tips make line contact along the wave vector. However, the tips are not bonded or soldered to the walls to make the screen easily removable as opposed to the permanently fixed wavy plate fins. The screen insert thus can retrofit an existing channel construction without the internal fins, be modified or replaced with another screen, or be removed for maintenance. In addition, the densely packed pores in the high porosity screen promote local turbulences in the channel flow to enhance heat transfer with small influences on the form drag. Because of the line-contact and no bond between the heat transfer walls and screen, no conduction happens through the screen allowing the screen material to be insensitive to the channel heat transfer enhancement. The objectives of the present investigations are to experimentally determine the effects of the geometric features of the porous screen insert on the convective heat transfer and pressure penalty. The objectives also include some correlations between the thermal performance and screen geometry in the channel.

The majority of the past investigations in channels with the porous media and internal fins compare the heat transfer and pressure drop with those from the correlations in a smooth channel to estimate the enhancement in the thermal performance. The flow field and convective heat transfer in a channel filled partially and fully with conductive porous media are investigated by [3, 4] in the laminar Reynolds number flow regime. Heat transfer in the channel of [3, 4] increases as the blockage ratio of porous media decreases. The porosity, height, and spacing of the fins in the annular space of the double pipe heat exchanger of [5] influence the flow and heat transfer. The experimental results of [6] in a tube with the square perforated twisted tapes inserts show the Nusselt number and friction factor increase by 6 and 8 folds, respectively, compared to those in the smooth pipe. The recent investigations by [7-15] in the channels filled in partially or completely with the metal porous foams augment the heat transfer coefficient along with the friction factor and uniformity of flow temperature. The foams are soldered to the channel walls to be employed as the internal fins and the fluid flows through the foam pores and channel gaps. The results of the investigations in [7-15] depend on the foam material, porosity, and thickness. Channel flows through the periodic porous baffles in [16, 17] enhance the heat transfer coefficient depending on the baffle geometry and porosity as the baffles act as fins in the studies. However, the experiments of [18, 19] also enhance the heat transfer coefficients with small influences in the pressure drops in tubes when the metal mesh screens are employed periodically as inserts and allow flow through the screen pores. The perturbations in the wall boundary layer flows are primarily responsible for the thermal performance augmentations in tube flows of [18, 19]. The multi-layered perforated plates employed in parallel to the flow in Torri and Yang [20] form small turbulences near the wall to augment mixing and mass transfer in the channel. Mahmood et al. [21] and Cramer et al. [22] employ the wavy porous inserts in channels to utilize the advantages of near wall local turbulences of porous plates in [20] to augment the heat transfer coefficients with small increase in the friction factors. The limited effects of wavelength and porosity on the heat transfer and pressure drop in the channel flow are presented in [21, 22].

The previous studies in channel flows find the porous inserts, baffles, and metal foams augment heat transfer with significant pressure penalty. The requirements of high pumping power due to the pressure penalty render the applications of these heat transfer augmentation devices unsuitable in the heat transfer channels of some HVAC units, electronic cooling, and solar absorber panels. The moderate thermal performance in the investigations of [21, 22] shows potentials of the wavy porous screens in the applications of heat transfer augmentation requiring the low pressure penalty in the channel. The present investigations complement the work of [21, 22] by combining the effects of height, porosity, and period of the wavy screen as well as the Reynolds number on the convective heat transfer and pressure drop. Table 1 shows the geometry and Reynolds number ranges of the present investigations and previous studies. The present investigation reports measured Nusselt numbers, friction factors, and thermal performance index relating the heat transfer augmentation with the friction factor increase due to the wavy porous screens in the rectangular channel flow.

2. Experimental Setup and Methods

Figure 1(a) shows the open-circuit low speed wind-tunnel employed for the experiments. A low pressure fan installed at the tunnel exit as shown in the figure moves the air through channels under it's suction. The atmospheric air smoothly accelerates through the two-dimensional reduction before entering the 2.0 m long inlet-channel that develops the flow. Following the inlet-channel air enters the 0.5 m long test section and then the outlet section before flowing into a large plenum and two pipe sections. The channels have the same rectangular cross-section of a constant width of 203 mm with adjustable height from the exit of reducer-section to the inlet of outlet-plenum. All the walls leading to the outlet-plenum are made of commercial acrylic plate. The test section houses the removable inserts and measurement instrumentations. The 203 mm wide walls of the test section are replaceable to install the appropriate instrumentations and fittings for the measurements of pressure drop and heat transfer. The pipe-sections are metered with the ISO 5167 [23] orifice plate flange assemblies for the measurements of air flow rate. The pipe-section of small diameter (57 mm) is employed for the low $Re < 2000$ measurements and the large diameter (100 mm) is employed for the high $Re > 2000$

4

measurements. The ball valves are used to close and open a pipe-section as required. Cramer [24] provides further details on the experimental setup.

The mass flow rate and Reynolds number in the channels are controlled by the fan speed operated through a variable speed drive. The measured pressure difference across the orifice plate and Stolz's equation in [23] are applied in an iterative procedure to estimate the orifice discharge coefficients which vary between 0.59 and 0.62. Wall static pressure taps and thermocouple tips are inserted through the drilled holes along the wall thickness of one of the 203 mm wide walls of the test section. The drilled holes are located along the length of the wall at the half-width positions as demonstrated in [21, 24]. Figure 1(b) illustrates the heater positions, insulations on the heated walls, and thermocouple positions in the wall and insulation layers. The test-wall of 203 mm wide with the pressure taps has a thickness of 12 mm for the pressure measurements. The same test-wall of 203 mm wide is then replaced with a test-wall of thickness 6 mm instrumented with the heaters, insulations, and thermocouples for the heat transfer measurements. Kapton^{TM} encapsulated thin foil heaters from a commercial source are pasted on the flow side of both of the 203 mm wide walls of the test section as in Fig. 1(b) and are in contact with the thermocouple tips. The heater covers only the full length of the test-wall and does not extend upstream or downstream of the test section. The etched foils in the heater provide a constant heat flux into the air stream when powered with a DC power source. The pressure taps are connected to a differential pressure transducer via a multi-port scanner using the plastic tubing. The orifice pressure-differences are obtained with the separate differential pressure transducers. The transducers are then connected to a National Instrument^{TM} data acquisition system. The thermocouples are connected directly to the multi-channel modules of the National Instrument^{TM} data acquisition system. Thermocouples are also placed between the insulation layers covering the test section as shown in Fig. 1(b) to measure the conduction losses during the heat transfer tests. The instrumentations of the test section are detailed in [21, 24].

The analogue signals from each pressure transducer are digitized at a sampling rate of 100 Hz for 2 sec and then time averaged. The signals from each thermocouple are sampled at 2 kHz for 2 sec

5

to time average. A Labview^{TM} program records all the signals for the time averaging. The time-averaged signals are then converted into the pressure and temperature units applying the appropriate calibrations. The power input to the heater is obtained from the applied voltage and current from the DC source and is adjusted based on the air mass flow rate to maintain a minimum difference of 10 °C between the bulk-mean temperature of air flow and wall temperatures. Equation (1) estimates the bulk-mean temperature along the heated test section based on the energy balance between the inlet ($x = 0$) and a streamwise location x. The inlet temperature, $T_{a,in}$ in the equation is the same as the ambient temperature of the unheated upstream air. The convective power, $Q_{c,x}$ (from $x = 0$ to x) is estimated after subtracting the conduction losses from the total power supplied to the heater. The quantity $\sum Q_{c,x}$ is used in Eq. (1) when the two walls of the channel are heated. The conduction losses are estimated with the measured temperature differences across the insulation layers [21, 24] and amount to a maximum of 3% of the total heater power. The etched foil element of the heater is designed to provide the constant power flux. The local convection heat flux is thus assumed to be almost constant. The local Nusselt number, Nu_x at each thermocouple position is then determined by Eq. (2) where $T_{w,x}$ is the wall temperature at the thermocouple location under consideration. The quantity, $Q_c/(L.W)$ indicates the average convective heat flux into the air stream.

$$T_{m,x} = T_{a,in} + \frac{\Sigma Q_{c,x}}{\left(m_a . C_p\right)} \tag{1}$$

$$Nu_x = \frac{\left(Q_c . D_h\right)}{\left[(L.W) . \left(T_{w,x} - T_{m,x}\right) . k_a\right]} \tag{2}$$

3. Mesh-Screen Geometry

The wavy inserts are fabricated from the commercially available flat screens made of grade 304 stainless steel wire-mesh. The mesh in the screen is created by interweaving the steel wires of diameter 0.28 mm and has a square shaped pore-aperture. Only two types of mesh screens of porosity 48% and 68% having the same wire diameter and square aperture could be obtained from the commercial sources. The effects of wire diameter and aperture shape are significant on the channel

6

thermo-hydraulic performance [22] and are not present objectives. The square size and number of pores per 25.4 mm in the flat mesh-screens are 0.57 mm and 31, respectively, for the 48% porosity mesh and 1.31 mm and 16, respectively, for the 68% porosity mesh. The waves of the inserts are fabricated by bending the mesh screens to the required profiles with custom-made sinusoidal jigs [22]. Two heights of the sinusoid are employed: 5 mm and 14 mm. Figure 2 shows an image of actual mesh-screen tested as well as the wave geometry of the screens. In total, twelve wavy screens are formed and tested as shown in Table 1 which also compares the geometry with the wavy screen of [21]. Each porosity of the 1st column uses all the wavelengths of the 2nd column. Two wavy screens are also formed with the $H = 14$ mm and irregular wavelengths between 20 mm and 12 mm for the 48% and 68% porosity. The screens in the 2nd row of the table are also tested by [22]. The streamwise length of the screens along x (Figure 2) covers only the test section. The geometry of the mesh pores remains about the same before and after bending of the screens except at the bend locations. The screen is inserted into the test section by removing and replacing a 203 mm wide wall. As indicated in Section 1, the wave tips are only in line-contact with the walls along the wave vector without any bond to allow for the screen to be replaced by a new one in the same test section. The screen material thus does not take part in the heat transfer from the wall. The contact between the wave tips and walls at all the locations is not significant due the manufacturing tolerances [22].

4. Uncertainty Estimates

The accuracy of the thermocouple is 0.1 °C and of the pressure transducer is 2 Pa. The major bias errors in the measurements are accounted for in the calibrations. The analyses of the precision and total uncertainties in the calibration, measurements, and estimations follow [25, 26]. The details of uncertainty estimates are provided in [24]. The uncertainties in the pressure are between 2.5 Pa and 13.0 Pa and mass flow rate are 2% or lower. The uncertainties in the calculated f are then between 2% and 8%. The maximum uncertainty in the temperature is 1.0 °C, heat flux is 4%, and Nusselt number is 7%. The changes in the results due to screen manufacturing tolerances, average heat flux variations as the Re changes, axial conductions, and repeated tests fall within the estimated

uncertainties [22, 24]. Also, the screen is heated only by the hot air which can reach 40 °C at the maximum near the end of the test-section for all the test conditions. The wall-heaters do not heat the screen directly at the line-contact positions between the wave-tips and heaters. Thermal expansion of the steel wire of the screen mesh due to the maximum temperature rise of about 18 °C from the ambient condition is then insignificant and any deformation of the screen geometry is neglected. The repeated Nu results for a screen at a given Re with three different heat flux levels presented in [24], which are not reproduced here for brevity, also confirm no effects of thermal deformation of the screen.

5. Discussions of Results

Experimental data are obtained as the flow reaches the steady state considered when the pressure and temperature vary within ±2 Pa and ±0.1 °C, respectively, over a 10 minute period. The Reynolds number varies between 400 and 35000. The constant heat flux boundary condition is applied at the heated wall with the suitable level of heat flux as dependent upon the Re. The air properties are estimated at the test section inlet conditions as the air pressure and temperature change by less than 1 kPa and 20 °C, respectively, from the inlet to exit of the test section. The experimental friction factors and Nusselt numbers are normalized by the baseline results measured in the same test section without the screen (smooth channel). The walls are adiabatic without any heating for the pressure drop tests.

5.1. Pressure Drop and Friction Factor

The normalized pressure drop, ΔP^* in the streamwise direction along test section, x/L is shown in Fig. 3 for the inserts with $\zeta = 68$ % and $H = 14$ mm. Results are shown for the wave periods, $\lambda = $ (12 mm, 20 mm) at Re = (1000, 6000). Equation (3) is used to determine ΔP^* from the measured wall static pressures, p_x. The reference pressure, p_0 in the equation is obtained on the wall 30 mm upstream of the test section. The inlet of test section is located at $x/L = 0$. The distributions of ΔP^* in Fig. 3 for a given λ decrease as the Re increases and for a given Re decrease as the λ increases. The flow blockage in the channel decreases as the wave period increases reducing the total number of waves and pressure drop (p_x - p_0). The straight lines through the data points indicate the least square fit by

8

the linear regression analysis. The line fits through the data points at $x/L \geq 0.40$ for a screen as the slope of the line is almost constant. The value of correlation coefficient is 0.99 for the line-fits. The slope values of the line-fits are also indicated inside the plots and can be compared between the inserts due to the change in Re and λ. The flow can be considered hydrodynamically fully-developed in the screen channel at $x/L \geq 0.40$ which is also reported by [22] irrespective of wavy insert (λ, ζ).

$$\Delta P^* = \frac{(p_x - p_0)}{0.5\rho V^2} \tag{3}$$

The friction factor, f in the channel is estimated from Eq. (4) and using the slopes of pressure drop distributions ($\Delta p/\Delta x$) along the channel. The values of $\Delta p/\Delta x$ for the screens are obtained from the line-fit slopes as those in Fig. 3. The friction factors for the inserts with $H = 14$ mm and $\zeta = 68\%$ and 48% are presented in Fig. 4(a) and Fig. 5(a), respectively, as the Re varies. The distributions of f in general decrease as the Re increases for all the inserts in two regimes: (i) a sharp and large decrease in f when $Re < 2000$ and (ii) a moderate asymptotic decrease in f when $Re > 2000$. The differences between the two distribution regimes of f are more prominent for the $\zeta = 48$ % inserts in Fig. 5(a) than for the $\zeta = 68$ % inserts in Fig. 4(a). The viscous friction dominates in the regime when $Re < 2000$ and the profile drag dominates in the regime when $Re > 2000$ due to the high turbulences. The figures also show that the f reduces with the flow blockage when the λ increases at a Re. The friction factors for the inserts with $H = 5$ mm are provided in [22].

$$f = \frac{(\Delta p/\Delta x)(D_h/4)}{0.5\rho V^2} \tag{4}$$

The effects of wave period on the friction factor for all the inserts are further illustrated in Fig. 4(b) and Fig. 5(b). The Δf in the figures is the difference of friction factors ($f_{\lambda=12}$ - $f_{\lambda>12}$) between the $\lambda = 12$ mm insert and $\lambda > 12$ mm insert and estimates the reduction in pressure drop when $\lambda > 12$ mm compared to the $\lambda = 12$ mm insert. The subscripts in λ in the plot-legend box indicate the corresponding wave period. The wave period of the λ_{Irr} insert varies between 12 mm and 20 mm. Figure 4(b) presents Δf for the inserts with $\zeta = 68\%$ and Fig. 5(b) presents Δf for the inserts with $\zeta =$

9

48%. The values of Δf decrease as the Re increase in both figures and fall very sharply when $Re <$ 7000. As the fluid pumping power in the channel is proportional to the pressure drop, the Δf decrease for the higher periods of the inserts is very desirable. The positive values Δf in both figures for an insert with $\lambda > 12$ mm are almost constant at $Re > 10000$ signifying no further reduction in the pressure penalty at high mass flow rates. The maximum Reynolds number of 11000 can be achieved with $H =$ 5 mm. Note, the Δf for the inserts with irregular wave periods (λ_{Irr}) and 20 mm period (λ_{20}) apparently follow the same distributions.

Figures 6(a) and 6(b) present the effects of screen porosity on the friction factors at different Reynolds numbers for $H = 14$ mm and $H = 5$ mm, respectively. The effects are shown by the differences in friction factors (Δf) as the porosity increases from $\zeta = 48\%$ to $\zeta = 68\%$ for all the wave periods. The subscripts in ζ in the plot-legend boxes in the figures indicate the porosity of the corresponding inserts with the same λ. The friction factor $f_{\xi=68\%} > f_{\xi=48\%}$ when $\Delta f < 0.0$ and $f_{\xi=68\%} <$ $f_{\xi=48\%}$ when $\Delta f > 0.0$. The values of Δf decrease sharply from negative toward 0.0 as the Re increases when $Re < 5000$ in Fig. 6(a) and when $Re < 3000$ in Fig. 6(b). When $Re > 5000$ and $Re > 3000$ in Fig. 6(a) and Fig. 6(b), respectively, the values are mostly within $0.01 < \Delta f < 0.02$ for a λ. The high negative values of Δf at lower Re in both figures thus signify the increase in the pressure penalty with porosity at a given wave period due to increase in the local turbulence. When the Δf values of Fig. 6 are compared with those of Figs. 4(b) and 5(b) at the corresponding H, the effects of λ and flow blockage are apparently more significant than the effects of ζ and porosity induced turbulence at low Re.

The present experimental f for all the twelve inserts can be related to the variable parameters of (ζ, λ, H, Re) in Eq. (5) developed for two regions of Reynolds number. The constants (A, B, C, D) in the equation equal to (0.050, -0.880, 6.987, -0.473), respectively, in the range of $400 < Re < 4000$ and (-0.600, -0.800, 1.090, -0.265), respectively, in the range of $4000 < Re < 35000$. The values from the correlation, f_{corr} in Eq. (5) are then plotted against the experimental values, f_{exp} in Figs. 7(a) and 7(b). The $\pm 15\%$ on the dashed lines in the plots indicates the deviation of 15% from the solid line (f_{corr}/f_{exp}

= 1). The correlated values differing from the experimental values outside the limits of ±15% fall mostly in the region of $2000 < Re < 4000$. Note the correlation in Eq. (5) is independent of the length of insert (L) as the experimental friction factor is obtained based on the constant ($\Delta p/\Delta x$) in the fully developed region. Equation (5) is valid for all the parameters in Table 1.

$$f_{corr} = \zeta^A \left(\frac{\lambda}{H}\right)^B C(Re)^D$$

(5)

5.2. Nusselt Numbers

The local Nusselt number, Nu_x distributions along x/L in the test section at $y/W = 0.5$ for the two-wall and one-wall heated boundary condition are shown in Fig. 8 (a) and (b), respectively. Equations (1) and (2) estimate the Nu_x from the measured wall temperatures and average heat flux. The data are presented for two inserts with λ = (12 mm, 20 mm) and H = 14 mm at Re = 1000 and 6000. The boundary condition of one-wall heating is applicable for the side channels of multi-channel flat plate heat exchangers, absorber panels of solar heaters, and cooling channels in the electronic components. For an insert at a Re in either Fig, 8(a) or 8(b), the distribution of Nu_x decreases at $x/L \leq 0.30$ where the flow thermally develops which is also shown by [22] irrespective of (λ, ζ) of the wavy insert. The Nu_x distribution then becomes almost constant along $x/L > 0.30$ in the thermally developed region. The Nu_x distribution for an insert also decreases with Re primarily because the flow turbulence decreases. The Nu_x values in the upstream developing section are important for the applications that employ smaller lengths of heat transfer channels.

The Nu_{avg} in Fig. 9(a) at different Re are the arithmetic averages of the local Nusselt numbers in the developed region. The distributions of Nu_{avg} shown for all three inserts with H = 14 mm and ζ = 68% increase with the Re. The decrease in the average value (ΔNu_{avg}) as the period increases i.e., when $\lambda > 12$ mm at a Re and wave height (H) is then presented in Fig. 9(b) to highlight the effects of wave period. The subscripts in λ in the legend box indicate the wave period and λ_{Irr} has wave periods varying between 12 mm and 20 mm. The ΔNu_{avg} distributions in Fig. 9(b) are within $-1 < \Delta Nu_{avg} < 11$ which is about ($\Delta Nu_{avg}/Nu_{avg}$) = 20% or lower of the corresponding average Nu_{avg} at $Re < 10,000$

11

and is about ($\Delta Nu_{avg}/Nu_{avg}$) = 10% or lower of the corresponding Nu_{avg} at $Re > 10,000$. For the inserts with $H = 5$ mm, the maximum achievable Re is 11,000. The Nu_{avg} decreases as the λ increases at the given (H, ξ, Re) primarily because the flow velocity reduces. The moderate change in λ does not apparently influence the local turbulence to affect the Nusselt numbers. The effects of wave period for the $\zeta = 48\%$ inserts on the average Nusselt numbers, Nu_{avg} at different Re are presented in Fig. 10. The difference in the average, ΔNu_{avg} in Fig. 10(b) is now within $-3 < \Delta Nu_{avg} < 8$ corresponding to about ($\Delta Nu_{avg}/Nu_{avg}$) = 30% or lower at $Re < 10,000$ and to about ($\Delta Nu_{avg}/Nu_{avg}$) = 6% or lower at $Re > 10,000$. In both Figs. 9(b) and 10(b), the small values of ΔNu_{avg} about 0.0 correspond to small percent of ($\Delta Nu_{avg}/Nu_{avg}$) when $\lambda > 12$ mm for the $H = 5$ mm inserts and for the λ_{Irr} insert. The effects of regular wave period of the inserts on the Nu_{avg} are thus significant at $Re < 10,000$ when $H = 14$ mm. Cramer et al. [22] report the detail Nu distributions for the inserts with $H = 5$ mm and two-wall heating.

The ΔNu_{avg} distributions in Figure 11 show the effects of porosity and signify the decrease in the Nusselt number when $\Delta Nu_{avg} > 0.0$ as the ξ increases from 48% to 68% for the six inserts with $H = 14$ mm and for the four inserts with $H = 5$ mm. Both the walls in contact with the insert tips are heated for the results. The subscripts in ξ in the legend-box indicate the porosity corresponding to a wave period, λ. The few values of $\Delta Nu_{avg} < 0.0$ in Fig. 11 indicate the increase in Nu_{avg} i.e. $Nu_{\xi=68\%} > Nu_{\xi=48\%}$ with ξ at a given Re and λ. However, all the ΔNu_{avg} values in Fig. 11(a) correspond to ratio ($\Delta Nu_{avg}/Nu_{avg}$) $\leq 12\%$ of the $Nu_{avg,\xi=48\%}$. The values in Fig. 11(b) correspond to $12\% < (\Delta Nu_{avg}/Nu_{avg})$ $< 16\%$ of the $Nu_{avg,\xi=48\%}$ for $Re > 5000$ and almost negligible for $Re < 3000$. Comparing the values of ΔNu_{avg} of Fig. 11 to those of Figs. 9(b) and 10(b) at the $H = 14$ mm, the effects of λ are more significant than the effects of ξ on the Nusselt number for most of the Re. The effects of λ and ξ on the Nusselt number at $H = 5$ mm are marginal for all the Re tested.

The average Nusselt numbers with the two-wall heating boundary condition for all the twelve inserts can be put into a functional relationship with (ζ, λ, H, Re) by Eq. (6) developed for two regions of Reynolds number. The constants (A, B, C, D) of Eq. (6) are (-0.300, -0.340, 0.410, 0.499),

respectively, in the range of $400 < Re < 4000$ and (-0.180, -0.220, 0.162, 0.624), respectively, in the range of $4000 < Re < 35000$. The equation is independent of the length of insert (L) as the Nu_{avg} values are obtained for the thermally developed region. The values of the function, Nu_{corr} are plotted against the experimental values, Nu_{exp} in Figs. 12(a) and 12(b) for all the inserts. The Nu_{exp} values are the same as Nu_{avg}. An upper limit of +15% and a lower limit of -15% of the ($Nu_{corr}/Nu_{exp} = 1$) solid line are shown by the dashed lines in the figures. All but few Nu_{corr} data in the range of $2000 < Re < 4000$ are bounded by the ±15% limit of Nu_{exp} in Fig. 12. Equation (6) is valid for all the parameters in Table 1.

$$Nu_{corr} = \zeta^A \left(\frac{\lambda}{H}\right)^B C(Re)^D$$

(6)

Figure 13 to Figure 16 present the average Nusselt number results with the one-wall heating boundary condition for all the twelve inserts. The average values are obtained from the local Nu distributions in the fully developed region at $x/L > 0.40$. The effects of Re on the Nu_{avg} are about the same in Fig. 13(a) and Fig. 14(a) for $\zeta = 68\%$ and $\zeta = 48\%$ inserts, respectively, as the Nu_{avg} increases by almost 11 times when the Re increases from 400 to 30000. The effects of wave period on the Nusselt number as the λ increases from 12 mm (λ_{12}) to 16 mm (λ_{16}) and 20 mm (λ_{20}) are presented by ΔNu_{avg} in Figs. 13(b) and 14(b). The value of ΔNu_{avg} at a Re is determined from the difference ($Nu_{avg,\lambda=12}$ - $Nu_{avg,\lambda>12}$) for the corresponding (H, ζ) of an insert. The average Nusselt number thus increases with the $\lambda > 12$ mm when $\Delta Nu_{avg} < 0.0$. Relative to the $Nu_{avg,\lambda=12}$ the values of ΔNu_{avg} are about 12% or lower for the inserts with regular wave period in both Figs 13(b) and 14(b). When the insert with irregular wave periods (λ_{Irr}) is employed, the Nusselt number changes significantly and the ΔNu_{avg} values are between 19% and 60% relative to the $Nu_{avg,\lambda=12}$ depending on the Re. The distributions of the average Nu for the $H = 5$ mm inserts are presented in detail by [22].

Figures 15 (a) and (b) show the effects of porosity on the average Nu by ΔNu_{avg} for the inserts with $H = 14$ mm and $H = 5$ mm, respectively. The value of ΔNu_{avg} at a Re is determined from the difference ($Nu_{avg,\zeta=48\%}$ - $Nu_{avg,\zeta=68\%}$) as the ζ increases from 48% to 68% for the corresponding (H, λ)

of an insert. The average Nusselt number thus increases with the $\xi > 48\%$ when $\Delta Nu_{avg} < 0.0$ in Fig. 15. Almost all the ΔNu_{avg} values in Fig. 15(a) for the $H = 14$ mm inserts are 13% or lower and in Fig. 15(b) for the $H = 5$ mm inserts are 10% or lower of the $Nu_{avg,\xi=48\%}$ at the corresponding Re. Thus, comparing the data among Fig. 13 to Fig. 15 for the one-wall heating, the effects of regular (λ, ξ) of the inserts on the Nu_{avg} are small and comparable except for the irregular wave periods, λ_{Irr} of the insert. The average Nu values with the one-wall heating can also be correlated to (ζ, λ, H, Re) by Eq. (6) in the two ranges of Reynolds number. The constants (A, B, C, D) of Eq. (6) for the one-wall heating are now (-0.150, -0.010, 0.200, 0.543) in the range of $400 < Re < 4000$ and (-0.170, -0.100, 0.094, 0.658) in the range of $4000 < Re < 30000$. The values of Nu_{corr} from Eq. (6) are then plotted against the experimental values, Nu_{exp} in Fig. 16 to show the deviation of the correlation from the experiment. As indicated, the correlation Nu_{corr} data are mostly within the $\pm15\%$ limit of the experimental Nu_{exp} in Fig. 16.

5.3. Thermal Performance

The thermal performance of the wavy inserts in the channel is presented as the ratio of screen channel friction factor and average Nusselt number to smooth channel friction factor and Nusselt number $(f/f_0, Nu/Nu_0)$. The smooth channel f_0 and Nu_0 (both two-wall and one-wall heating) are measured in the empty channel without the insert at the corresponding Re and channel height (H) of the screen channel. The measured (f_0, Nu_0) are also obtained at the fully developed conditions. The friction factor ratio, f/f_0 signifies the increase in pressure drop and the Nusselt number ratio, Nu/Nu_0 signifies the increase in heat transfer coefficient when the insert is employed in the smooth channel at a given mass flow rate and channel height. Figure 17 presents the ratios f/f_0, Nu/Nu_0 with the two-wall heating, and Nu/Nu_0 with the one-wall heating. The legends of the data are provided on the top of plot in Fig. 17(b). The results are shown for the $H = 14$ mm inserts. The results for the $H = 5$ mm inserts are already shown in [22]. As shown in Fig. 17(a), the ratios f/f_0 increase significantly with the Reynolds number in $Re \leq 8000$ and then change little with the Re. The f/f_0 ratios also seem to decrease little as both (λ, ξ) of the inserts increase at a given (H, Re). Similar observations with the $H = 5$ mm

14

are presented in [22]. On the contrary, the ratios Nu/Nu_0 of Figs. 17 (b, c) increase significantly with the Reynolds number in $Re \leq 3000$, then decrease significantly as the Reynolds number increases in $4000 \leq Re \leq 16000$. Cramer et al. [22] show similar distributions of the Nu/Nu_0 ratios as the Re changes with the $H = 5$ mm inserts. The Nu/Nu_0 ratios change little when $Re > 16000$ in Figs. 17(b, c). The f/f_0 at $Re > 3000$ and the Nu/Nu_0 at all the Re are usually slightly higher for the insert with ($\xi = 48\%, \lambda = 12$ mm). The results of Nu/Nu_0 for an internal wavy porous plate-fin from [2] are included in Fig. 17(b) for comparisons.

The enhancement of heat transfer rate with pumping power for the wavy inserts as the mass flow rate changes in the channel can be presented by the thermal performance factor, $(Nu/Nu_0)/(f/f_0)^{(1/3)}$ as defined by Gee and Webb [27]. A performance factor (PF) value of higher than 1.0 then signifies three important design criteria on the factors heat transfer rate, fluid pumping power, and heat transfer surface area: (i) heat transfer rate increases as the other two factors are the same as in smooth channel, (ii) pumping power decreases as the other two factors are the same as in smooth channel, (iii) heat transfer area decreases as the other two factors are the same as in smooth channel. The performance factors (PF) for all the twelve inserts are shown in Fig. 18 as the Re changes and are mostly less than 1.0 and decrease as the Re increases beyond 3000 for both two-wall heating and one-wall heating. The performance factors in Mahmood et al. [21] are obtained with a high porosity wavy insert having a different wire diameter and pore geometry than those in the present inserts. The (PF) values of [21] are also less than 1.0 and compared with the 5 mm inserts in [22].

The dependence of (PF) for the two-wall heating on the (ζ, λ, H, Re) are given by Eq. (7) developed for the two regions of Reynolds number. The constants (A, B, C, D) of Eq. (7) have values of (-0.350, -0.090, 0.408, 0.1) in the range of $400 < Re < 2100$ and (-0.005, -0.150, 5.452, -0.214) in the range of $2100 < Re < 35000$. Equation (7) is also used for the one-wall heating in the two regions of Reynolds number. The values of (A, B, C, D) of Eq. (7) for the one-wall heating are now (-0.030, 0.200, 0.374, 0.108) in the range of $400 < Re < 4000$ and (0.100, 0.050, 5.700, -0.225) in the range of $4000 < Re < 30000$. The results of the correlated PF_{corr} from Eq. (7) are plotted against the

15

experimental PF_{exp} in Fig. 19 and Fig. 20. Most of the PF_{corr} values are within the ±15% limit of the PF_{exp} values in both the figures. The significant deviations of PF_{corr} outside of the ±15% limit in Fig. 19(b) occur when 1000 < Re < 3000. Equation (7) is valid for all the parameters in Table 1.

$$PF_{corr} = \zeta^A \left(\frac{\lambda}{H}\right)^B C(\text{Re})^D \tag{7}$$

6. Summary and Conclusions

Experimental results of the friction factor (f), average Nusselt number (Nu), and thermal performance (f/f_0, Nu/Nu_0, PF) are presented in a rectangular channel when the wavy porous mesh screens are employed as inserts in the air channel. The sinusoidal waves of the inserts are placed perpendicular to the flow with the wave tips in only point contact with the 203 mm wide walls of the channel without any bonding. Twelve inserts are tested as the length, porosity, and height of the waves are varied. The pores are square sized. The flow Reynolds number varies between 400 and 35000 based on the channel hydraulic diameter and mass flow rate. The constant heat flux boundary condition at the 203 mm walls is employed for the heat transfer measurements. The objectives of the investigation are to present the combined effects of wavelength (λ), porosity (ζ), and height (H) of the wavy insert as well as the Reynolds number (Re) on the measured results (f, Nu, f/f_0, Nu/Nu_0, PF). Experimental correlations are also presented to reasonably estimate the (f, Nu, PF) from the parameters (λ, ζ, H, Re). Most of the values of (f, Nu, PF) from the correlations are within ±15% of the corresponding experimental values.

- The effects of Reynolds number are the strongest, followed by the wavelength, and then porosity on the results. The friction factor (f) decreases significantly as the Re increases and the average Nu increases significantly with the Re irrespective of the (λ, ζ, H) of the wavy inserts. The results of (Nu/Nu_0, PF) increase only in the range of $Re < 3000$ and then decrease in $Re > 3000$. However, the f/f_0 increases in the rage of $Re < 8000$ and then change little in $Re > 8000$. The effects of wavelength and porosity on f are prominent in $Re < 7000$ when both the (λ, ζ) of the wavy insert increase. The effects of wavelength show the average Nu decreases

16

significantly as the λ increases for the inserts with the higher H in $Re < 10000$ when the two walls are heated. The effects of porosity on the Nu are marginal as the ξ increases irrespective of the (λ, H, Re) for the inserts when either the two-walls or one-wall is heated. The average Nu with the cases of one-wall heated changes significantly only when the wavelength of an insert changes from the regular to irregular period at a given (ξ, H, Re). The effects of (λ, ξ) on the (f/f_0) are more prominent than on the (Nu/Nu_0).

- The effects of (λ, ξ, H) of the inserts on the PF are the most prominent in the range of $1000 < Re < 3000$ when most of the PF values are either higher than or near to 1.0. The values of $PF > 1.0$ are desirable to increase the heat transfer rate, decrease the pumping power, and decrease the heat transfer surface area compared to those in the smooth channel.

- In overall, the operating range of $1000 < Re < 4000$ for the twelve wavy inserts provides the most desirable results on the pressure drop and thermal performance.

The wavy inserts are light weight, simple in constructions, cheap, easy to implement for new and retrofit applications, and good structural supports for the channel walls. The results presented are thus important for the design and improvement of thermal performance of the heat transfer channels.

Nomenclature

(A_c, D_h)	Channel cross-sectional area, hydraulic diameter
(C_p, k_a)	(Specific heat, thermal conductivity) of air
f	Friction factor in screen channel
(H, L, W)	(Height, length, width) of test section
m_a	Mass flow rate of air
Nu	Nusselt number
PF	Performance factor index, $(Nu/Nu_0)/(f/f_0)^{(1/3)}$
(p_x, p_0, P^*)	Pressure: local wall-static, reference, normalized on wall
$(Q_c, Q_{c,x})$	Convective power on surface: total, local (x = 0 to x)
Re	Reynolds number, $\left(\dfrac{m_a D_h}{A_c \mu_a}\right)$
$(T_{a,in}, T_{m,x}, T_{w,x})$	Temperature: inlet air, local bulk-mean of air, on wall at distance x
V	Mean flow velocity, $\left(\dfrac{m_a}{A_c \rho_a}\right)$
(X, Y, Z)	Cartesian coordinate system

Greek Symbols

Δ	Difference between two quantities
(μ_a, ρ_a)	(Dynamic-viscosity, density) of air
(λ, ζ)	(Wave period, porosity) of wavy screen

Subscripts and Superscripts

avg	average property
x	local property on the wall along x
0	reference or smooth channel property
Irr	Irregular wave period

References

[1] Webb, R. L., and Kim, N. -H., 2005, Principles of Enhanced Heat Transfer, 2nd ed., Taylor and Francis, Oxon, UK, pp. 57-60, 210-227, 246-269.

[2] Kays, W. M., and London, A. L., 1964, Compact Heat Exchangers, 2nd ed., McGraw-Hill, USA, pp. 155, 219.

[3] Jeng, T. -M., Tzeng, S. -C., and Tang, F. -Z., 2009, "Fluid Flow and Heat Transfer Charateristics of the Porous Metallic Heat Sink with a Conductive Cylinder Partially Filled in a Rectangular Channel," International J. Heat and Mass Transfer, **53**, pp. 4216–4227.

[4] Tong, T. W., Sharatchandra, M. C., and Gdoura, Z., 1993, "Using Porous Inserts to Enhance Heat Transfer in Laminar Fully-Developed Flows," International Communications in Heat and Mass Transfer, **20**(6), pp. 761–770.

[5] Kahalerras, H., and Targui, N., 2008, "Numerical Analysis of Heat Transfer Enhancement in a Double Pipe Heat Exchangerwith Porous Fins," International J. of Numerical Methods for Heat & Fluid Flow, **18**(5), pp. 593–617.

[6] Suri, A. R. S., Kumar, A., and Maithani, R., 2018, "Experimental Investigation of Heat Transfer and Fluid Flow Behaviour in Multiple Square Perforated Twisted Tape with Square Wing Inserts Heat Exchanger Tube," Heat and Mass Transfer, **54**(6), pp. 1813–1826.

[7] Alhusseny, A., Turan, A., and Nasser, A., 2015, "Developing Convective Flow in a Square Channel Partially Filled with a High Porosity Metal Foam and Rotating in a Parallel-Mode," International J. Heat and Mass Transfer, **90,** pp. 578-590.

[8] Chen, C. -C., Huang, P. C., and Hwang, H. Y., 2013, "Enhanced Forced Convective Cooling of Heat Sources by Metal-Foam Porous Layers," International J. Heat and Mass Transfer, **58,** pp. 356-373.

[9] Lu, W., Zhang, T., and Yang, M., 2016, "Analytical Solution of Forced Convective Heat Transfer in Parallel-Plate Channel Partially Filled with Metallic Foams," International J. Heat and Mass Transfer, **100,** pp. 718-727.

[10] Park, S. H., Kim, T. H., and Jeong, J. H., 2016, "Experimental Investigation of the Convective Heat Transfer Coefficient for Open-Cell Porous Metal Fins at Low Reynolds Numbers," International J. Heat and Mass Transfer, **100,** pp. 608-614.

[11] Wang, B., Hong, Y., Hou, X., Xu, Z., Wang, P., Fang, X., and Ruan, X., 2015, "Numerical Configuration Design and Investigation of Heat Transfer Enhancement in Pipes Filled with Gradient Porous Materials," Energy Conversion and Management, pp. 206-215.

[12] Kim, S. Y., Paek, J. W., and Kang, B. H., 2000, "Flow and Heat Transfer Correlations for Porous Fin in a Plate-Fin Heat Exchanger," J. Heat Transfer, **122**, pp. 572-578.

[13] Mohammadian, S. K., and Zhang, Y., 2016, "Temperature Uniformity Improvement of an Air-Cooled High-Power Lithium-Ion Battery Using Metal and Non-Metal Foams," J. Heat Transfer, **138**, pp. 1145021-1145024.

[14] Mohammadian, S. K., Rassoulinejad-Mousavi, S. M., and Zhang, Y., 2015, "Thermal Management Improvement of an Air-Cooled High-Power Lithium-Ion Battery by Embedding Metal Foam," J. Power Sources, **296**, pp. 305-313.

[15] Maerefat, M., Mahmoudi, S. Y., and Mazaheri, K, 2011, "Numerical Simulation of Forced Convection Enhancement in a Pipe by Porous Inserts," Heat Transfer Engineering, **32**(1), pp. 45-56.

[16] Santos, N. B., and de Lemos, M. J. S., 2006, "Flow and Heat Transfer in a Parallel-Plate Channel with Porous and Solid Baffles," Numerical Heat Transfer, Part A, **49**, pp. 471-494.

[17] Davari, A., and Maerefat, M., 2016, "Numerical Analysis of Fluid Flow and Heat Transfer in Entrance and Fully Developed Regions of a Channel with Porous Baffles," J. Heat Transfer, **138**, pp. 0626011-06260110.

[18] Pavel B. I., and Mohamad A. A., 2004, "Experimental Investigation of the Potential of Metallic Porous Inserts in Enhancing Forced Convective Heat Transfer," J. Heat Transfer, **126**, pp. 540-545.

[19] Pavel B. I., and Mohamad A. A., 2004, "An Experimental and Numerical Study on Heat Transfer Enhancement for Gas Heat Exchangers Fitted with Porous Media," International J. Heat and Mass Transfer, **47**, pp. 4939-4952.

[20] Torii, S. and Yang, W. -J., 2007, "Thermal-Fluid Flow Transport Phenomenon Over Slot-Perforated Flat Plates Placed in Narrow Channel," J. Thermophysics and Heat Transfer, **21**(2), pp. 346-351.

[21] Mahmood, G. I., Simonson, C. J., and Besant, R. W., 2015, "Experimental Pressure Drop and Heat Transfer in a Rectangular Channel With a Sinusoidal Porous Screen," J. Heat Transfer, **137**, pp. 0426011-04260111.

[22] Cramer, L., Mahmood, G. I., and Meyer, J. P., 2018, "Thermohydraulic Performance of a Channel Employing Wavy Porous Inserts," Heat Transfer Research, **49**(18), pp. 1867–1883.

[23] International Standard Organization, ISO 5167-1980(E), Measurement of Fluid Flow by Means of Orifice Plates, Nozzles and Venture Tubes Inserted in Circular Cross-Section Conduits Running Full, 1980-07-15.

[24] Cramer, L., 2018, "Enhancement of the Thermal Performance of Solar Heat Exchanges with Porous Inserts," M.Eng. thesis, University of Pretoria.

[25] Beckwith, T. G., Marangoni, R. D., and Lienhard, J. H., 2007, Mechanical Measurements, sixth ed., New Jersey: Pearson Prentice Hall, pp. 42-45, 54-59.

[26] Moffat, R. J., 1988, "Descibing the Uncertainty in Experimental Results," Experimental Thermal and Fluid Science, **1**(3), pp. 3-7.

[27] Gee, D. L., and Webb, R. L., 1980, "Forced Convection Heat Transfer in Helical Ribbed Tubes," International Journal of Heat and Mass Transfer, **23**(8), pp. 1127–1136.

Table Caption List

Table 1: Geometry of wavy screens and operating range

Figure Caption List

Fig. 1   Schematic plan view of: (a) experimental setup of wind tunnel, and (b) details of test section for heat transfer measurements including coordinates.
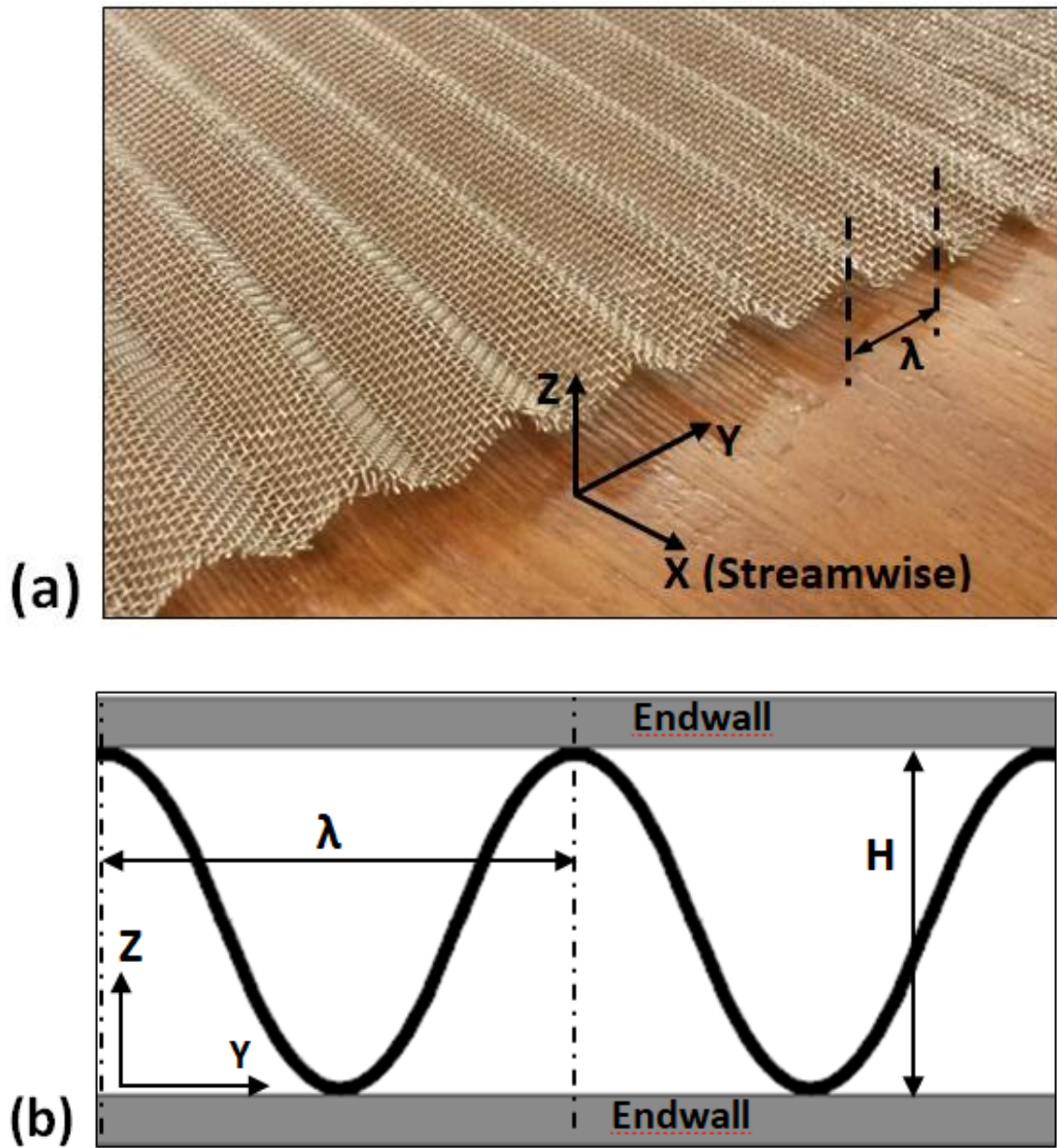
Fig. 2   (a) Image of an actual wavy mesh insert, and (b) Sinusoidal geometry of insert in the YZ plane (λ = wave period, H = wave height). Channel streamwise direction is indicated by X-coordinate.
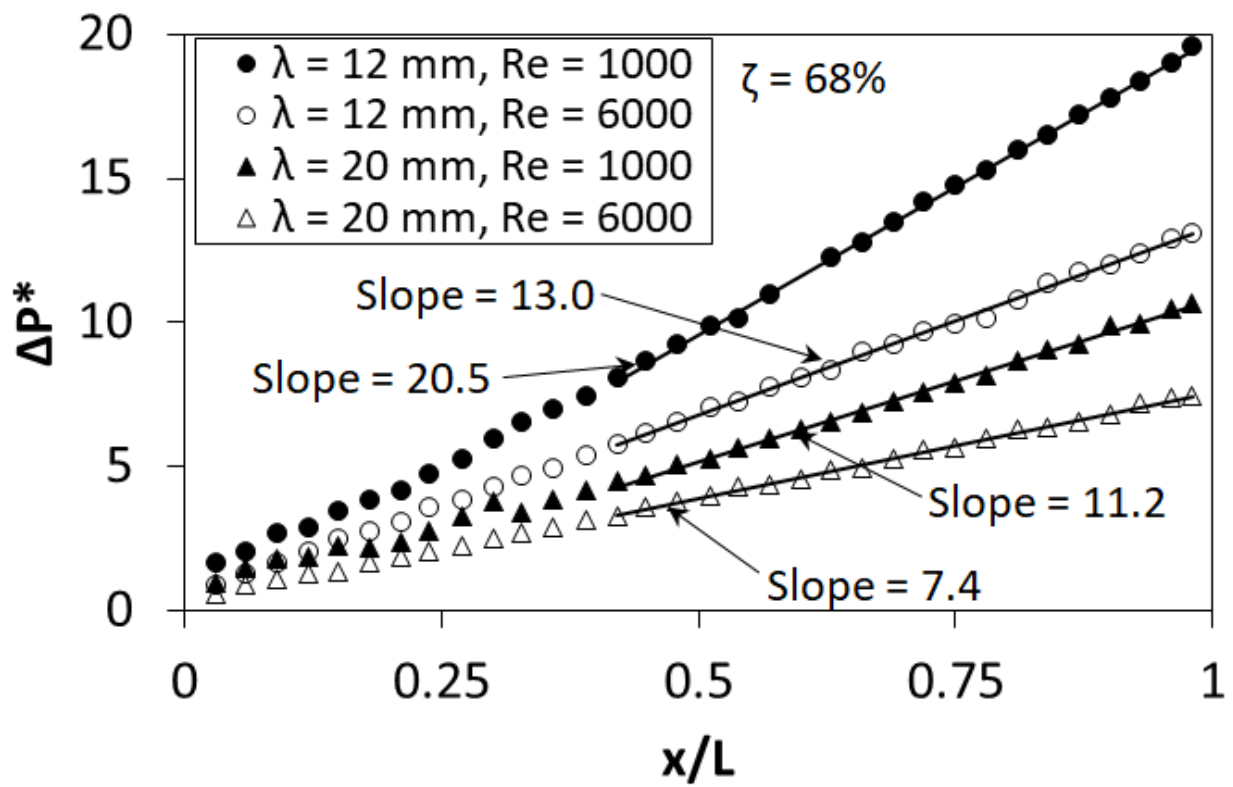
Fig. 3   Non-dimensional pressure drop (ΔP^{*}) along x/L for wavy screens with ζ = 68 %, H = 14 mm, and λ = (12 mm, 20 mm) for Re = (1000, 6000).

Fig. 4   Friction factor (f) at different Re for ζ = 68%: (a) H = 14 mm and λ = (12 mm, 16 mm, 20 mm), and (b) friction factor decrease, Δf with H = (14 mm, 5 mm) for increase in λ from 12 mm.
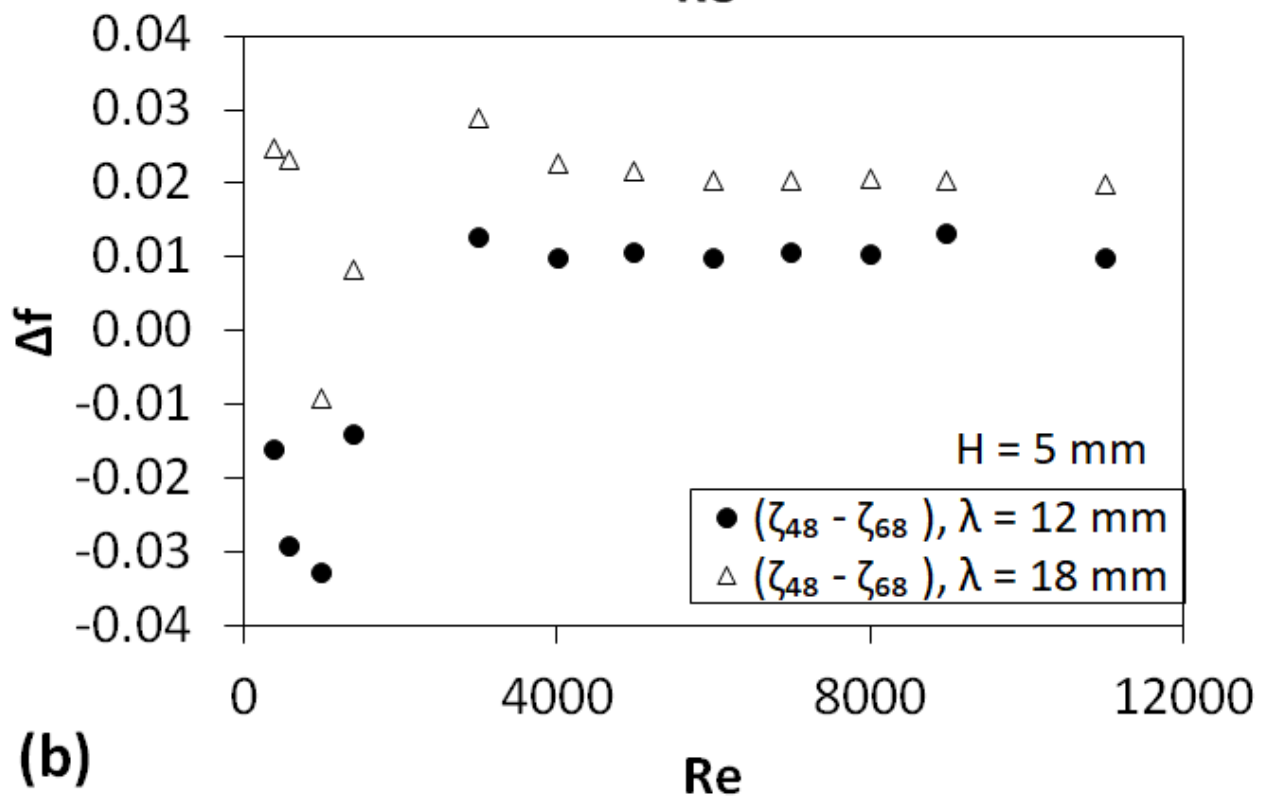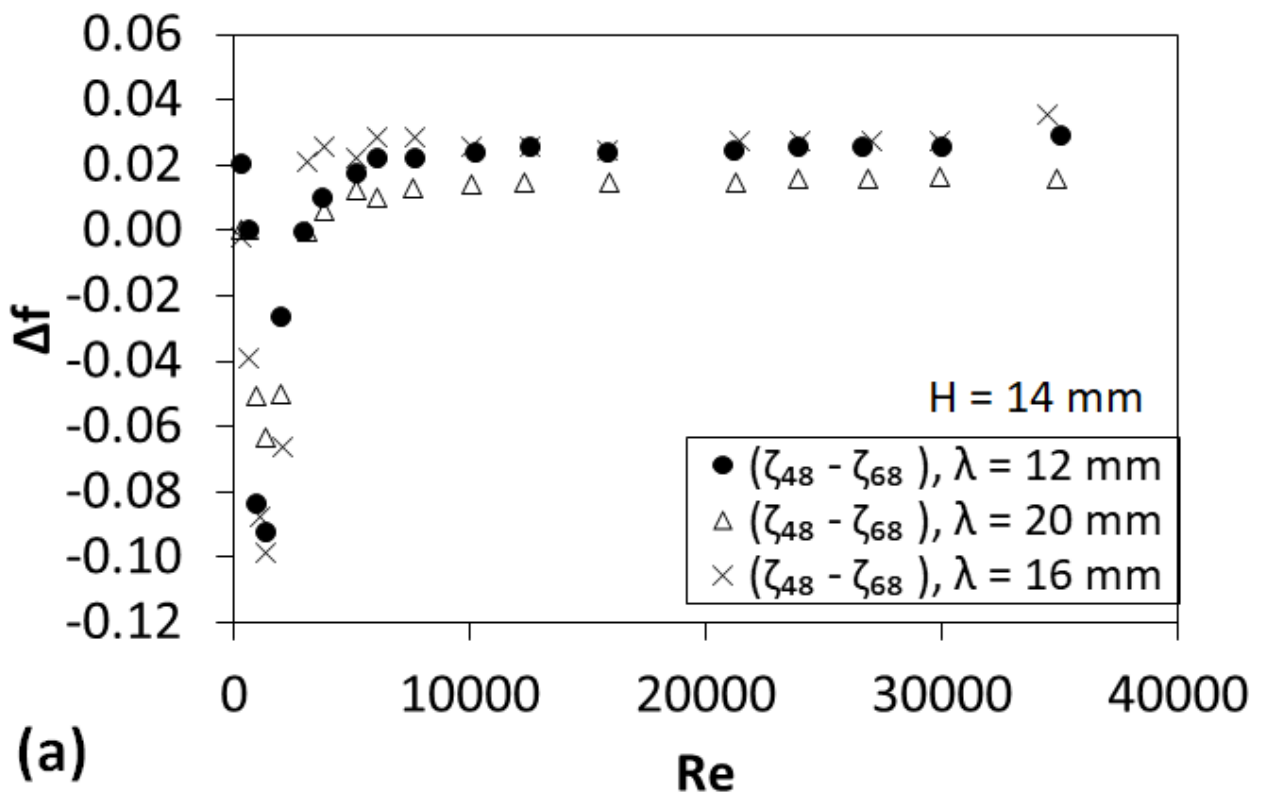
Fig. 5   Friction factor (f) at different Re for ζ = 48%: (a) H = 14 mm and λ = (12 mm, 16 mm, 20 mm), and (b) friction factor decrease, Δf with H = (14 mm, 5 mm) for increase in λ from 12 mm.

Fig. 6   Difference in friction factor (Δf) at different Re as insert ζ increases from 48% to 68% for: (a) H= 14 mm, and (b) H = 5 mm.
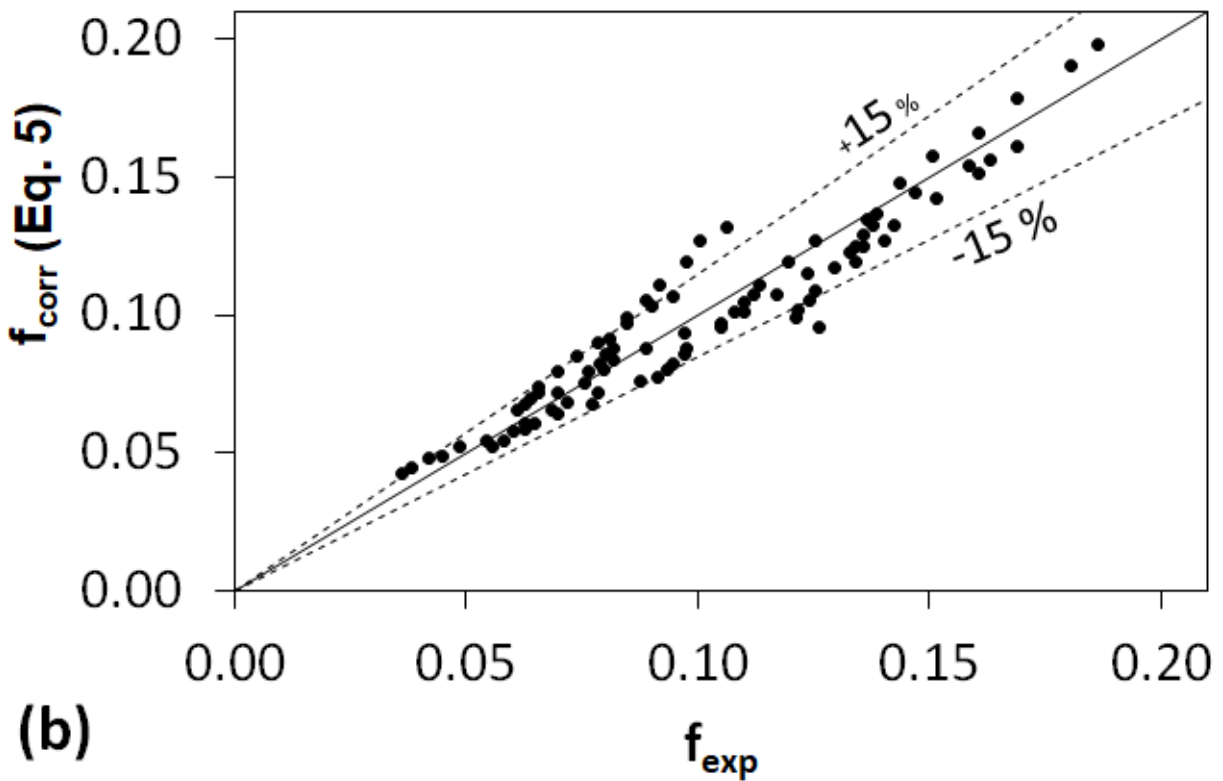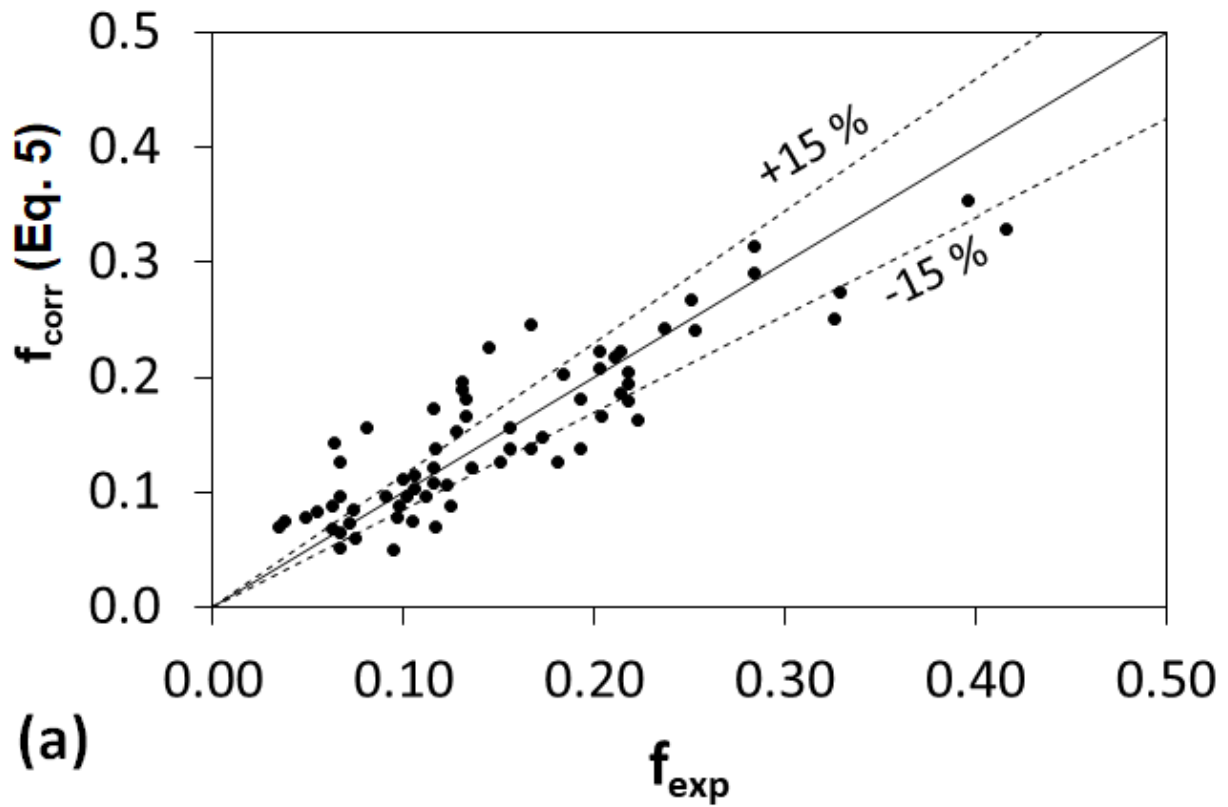
Fig. 7   Comparisons of friction factors from correlation, f_{corr} of Eq. (5) with those from experiments, f_{exp} for: (a) 400 < Re < 4000, and (b) 4000 < Re < 35000 (inclusive of all ζ, λ, H, Re).

Fig. 15   Decrease in average ΔNu_{avg} versus Re with one-wall heating as porosity, ξ increases from 48% to 68%: (a) H =14 mm, λ = (12 mm, 16 mm, 20 mm), and (b) H = 5 mm, λ = (12 mm, 18 mm).

Fig. 16   Comparisons of average Nusselt number from correlation with one-wall heating, Nu_{corr} of Eq. (6) with those from experiments, Nu_{exp} for: (a) 400 < Re < 4000, and (b) 4000 < Re < 35000 (inclusive of all ζ, λ, H, Re). Constants in Eq. (6) are different from those for two-wall heating.

Fig. 17   Performance of f and Nu_{avg} vs. Re relative to smooth channel for the H = 14 mm inserts: (a) f/f_0, (b) Nu/Nu_0 with two-wall heating, and (c) Nu/Nu_0 with one-wall heating.

Fig. 18   Performance factor (PF) as Re increases (inclusive of all ζ, λ, H) for: (a) two-wall heating and (b) one-wall heating.

Fig. 19   Comparisons of performance factor from correlation with two-wall heating, PF_{corr} of Eq. (7) with those from experiments, PF_{exp} for: (a) 400 < Re < 2100, and (b) 2100 < Re < 35000 (inclusive of all ζ, λ, H, Re).

Fig. 20   Comparisons of performance factor from correlation with one-wall heating, PF_{corr} of Eq. (7) with those from experiments, PF_{exp} for: (a) 400 < Re < 4000, and (b) 4000 < Re < 30000 (inclusive of all ζ, λ, H, Re). Constants in Eq. (7) are different from those for two-wall heating.

Table 2: Geometry of wavy screens and operating range

Porosity (ζ)	Wavelength (λ), mm	Wave height (H), mm	Operating range, Re
48%, 68%	20, 16, 12	14	$400 \leq Re \leq 35{,}000$
48%, 68% [22]	18, 12	5	$400 \leq Re \leq 11{,}000$
79.4% [21]	12.5	5	$1{,}300 \leq Re \leq 3{,}800$
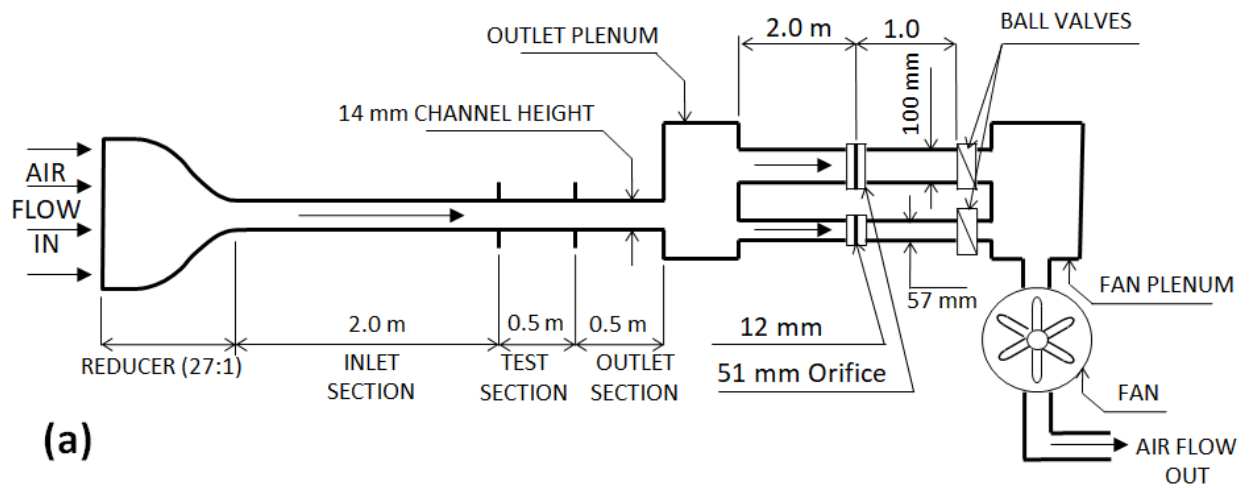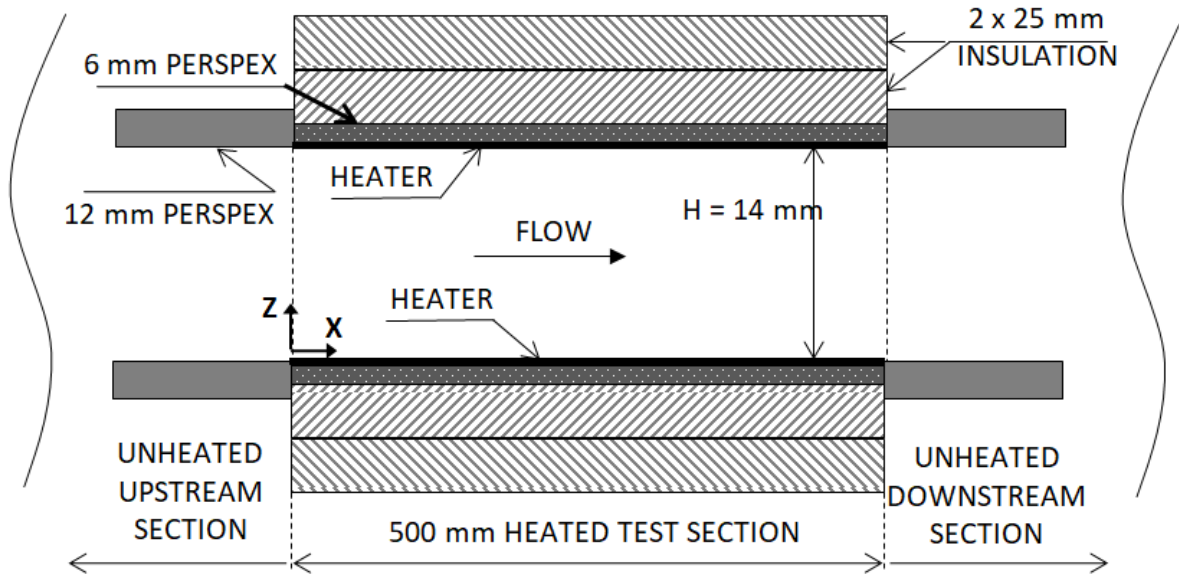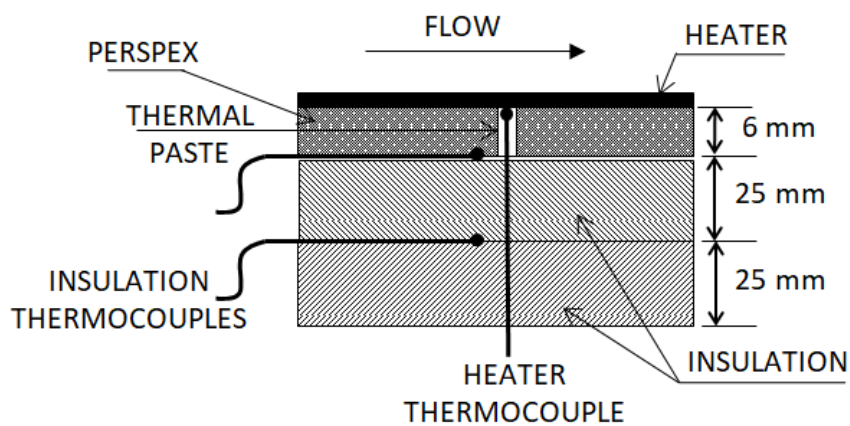
Figure 1: Schematic plan view of: (a) experimental setup of wind tunnel, and (b) details of test section for heat transfer measurements including coordinates.

Figure 2: (a) Image of an actual wavy mesh insert, and (b) Sinusoidal geometry of insert in the YZ

plane (λ = wave period, H = wave height). Channel streamwise direction is indicated by X-coordinate.

Figure 3: Non-dimensional pressure drop (ΔP^*) along x/L for wavy screens with $\zeta = 68$ %, H = 14 mm, and $\lambda = (12$ mm, 20 mm) for Re = (1000, 6000).
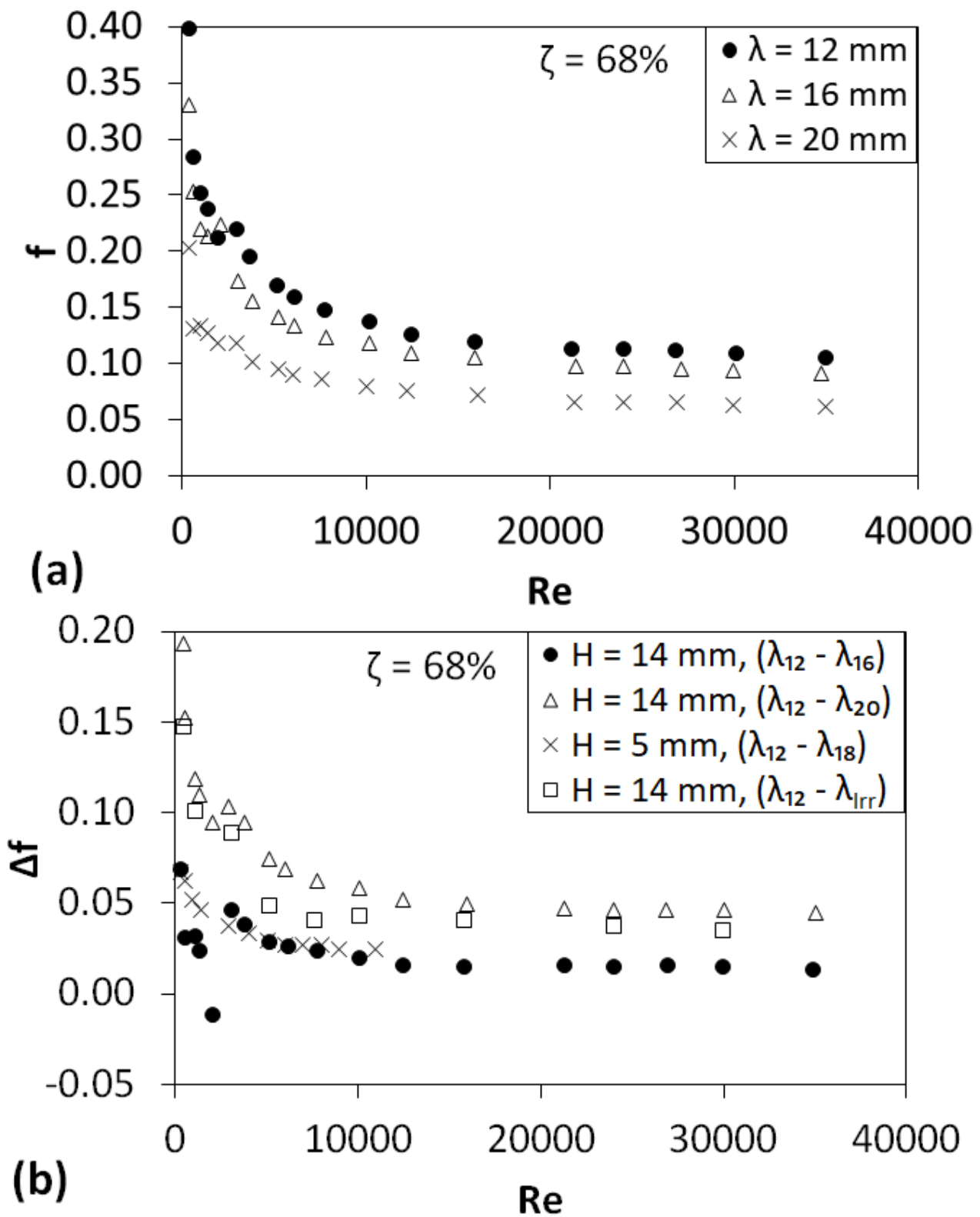
Figure 4: Friction factor (f) at different Re for ζ = 68%: (a) H = 14 mm and λ = (12 mm, 16 mm, 20 mm), and (b) friction factor decrease, Δf with H = (14 mm, 5 mm) for increase in λ from 12 mm.
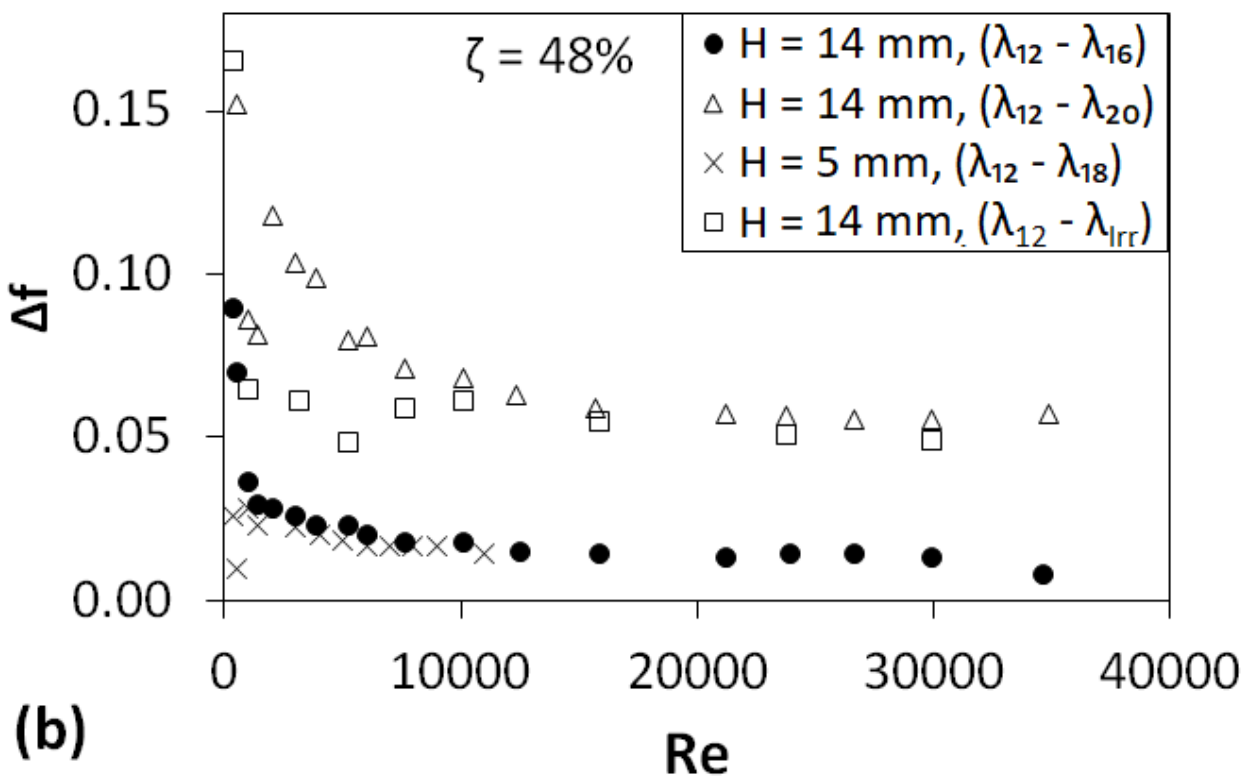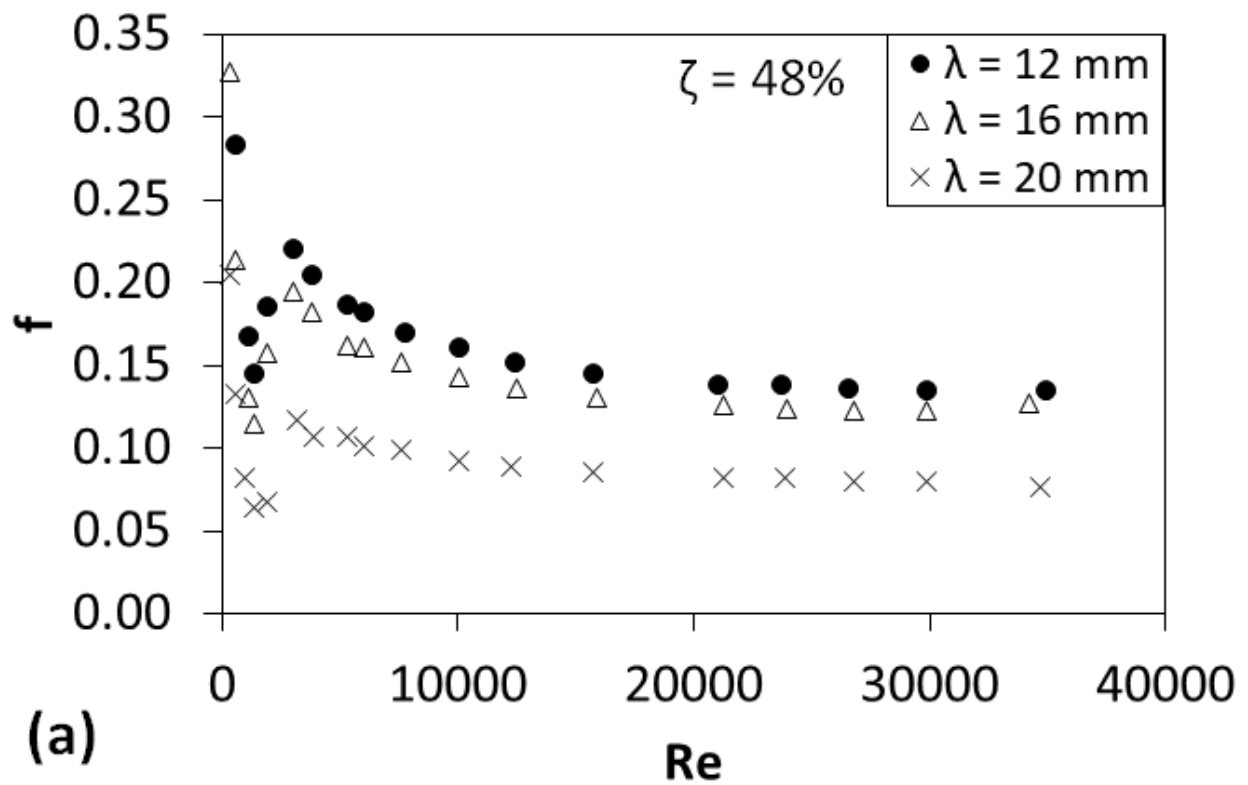
Figure 5: Friction factor (f) at different Re for ζ = 48%: (a) H = 14 mm and λ = (12 mm, 16 mm, 20 mm), and (b) friction factor decrease, Δf with H = (14 mm, 5 mm) for increase in λ from 12 mm.

Figure 6: Difference in friction factor (Δf) at different Re as insert ζ increases from 48% to 68% for:

(a) H= 14 mm, and (b) H = 5 mm.

Figure 7: Comparisons of friction factors from correlation, f_{corr} of Eq. (5) with those from experiments, f_{exp} for: (a) $400 < Re < 4000$, and (b) $4000 < Re < 35000$ (inclusive of all ζ, λ, H, Re).
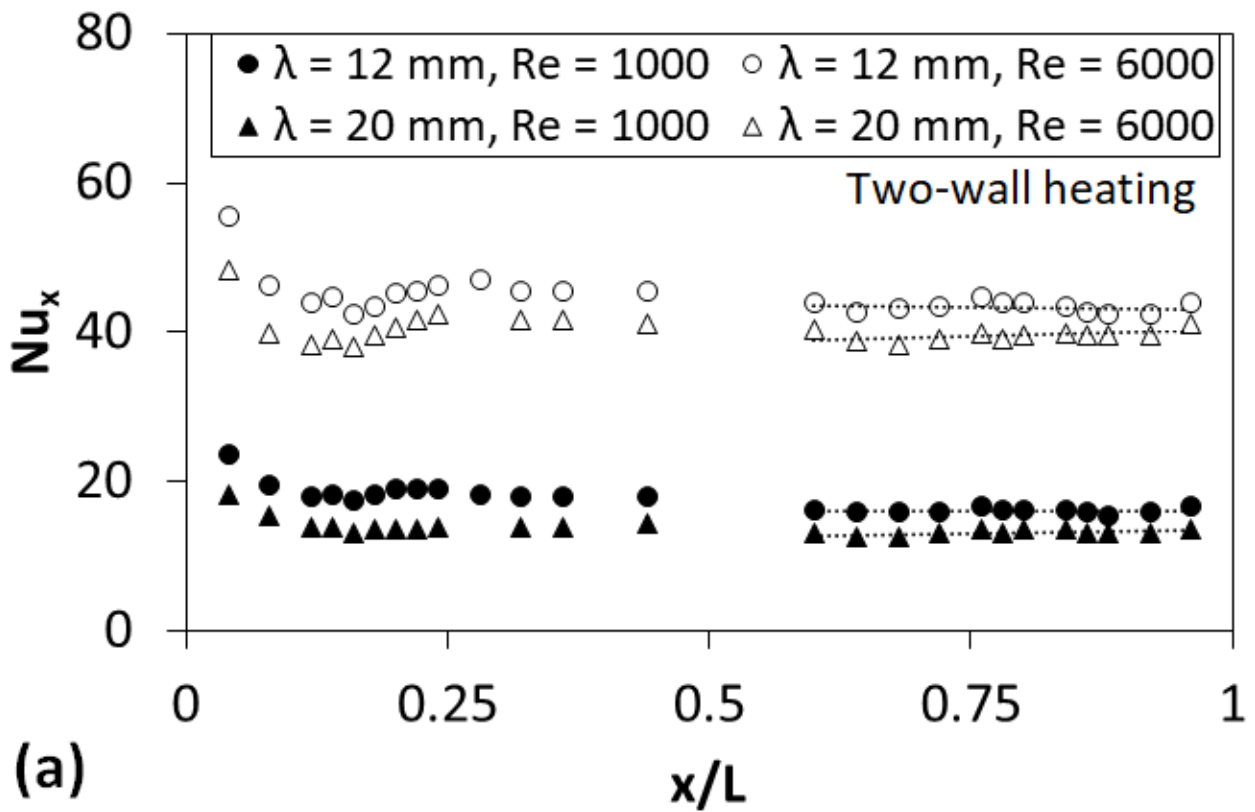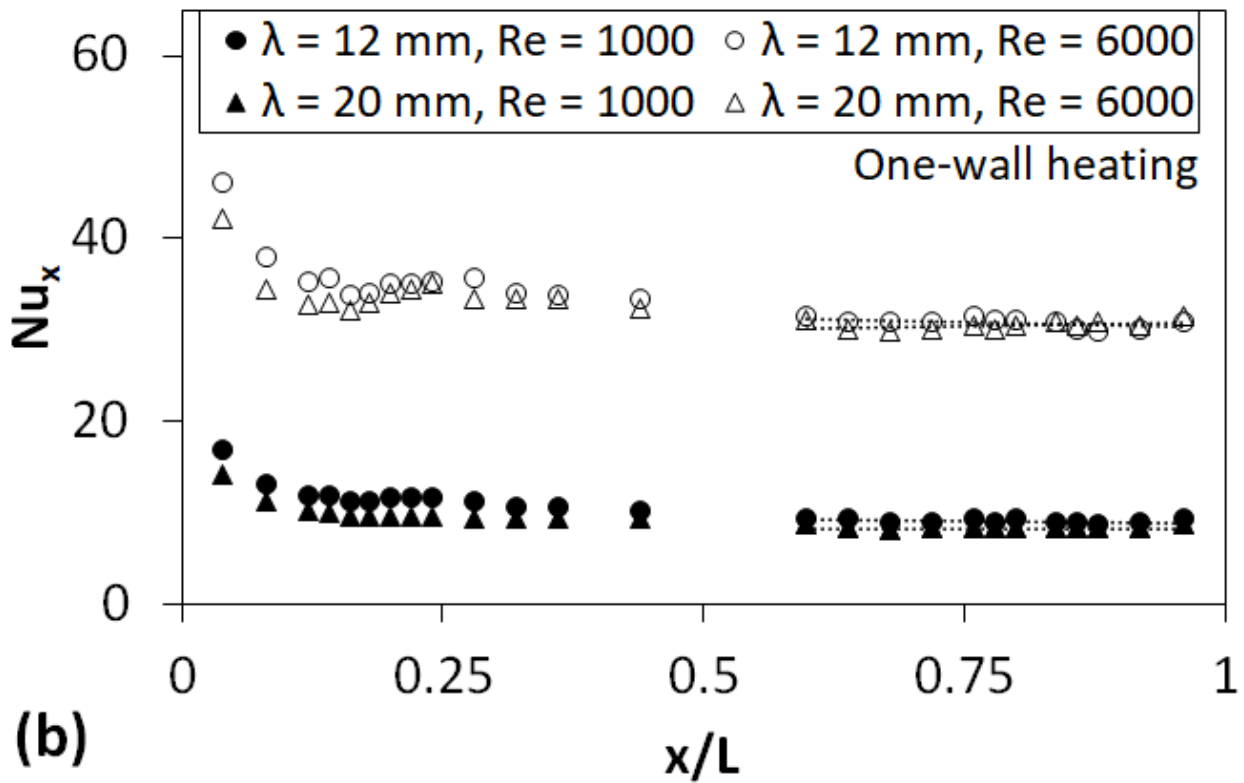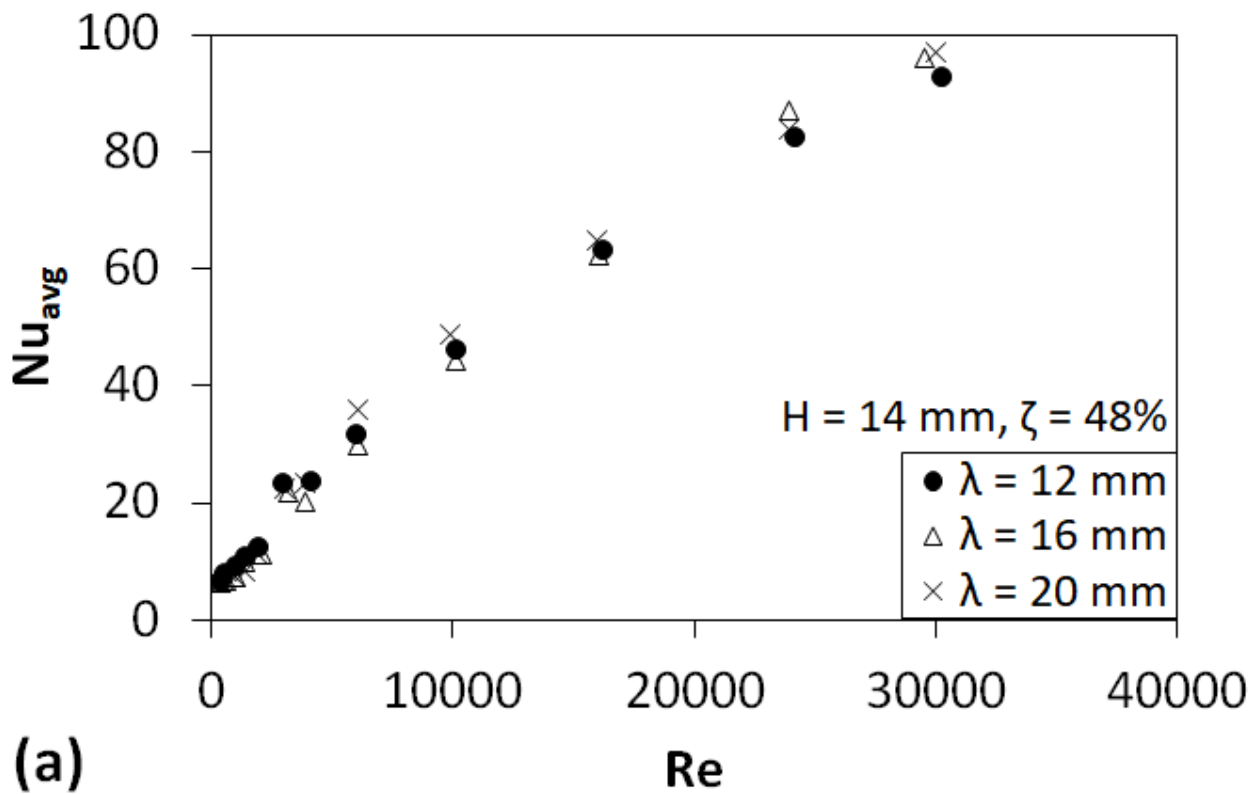
Figure 8: Local Nusselt numbers, Nu_x along x/L for the inserts with H = 14 mm, ζ = 68 %, and λ = (12 mm, 20 mm) at Re = (1000, 6000): (a) two-wall heating, and (b) one-wall heating.
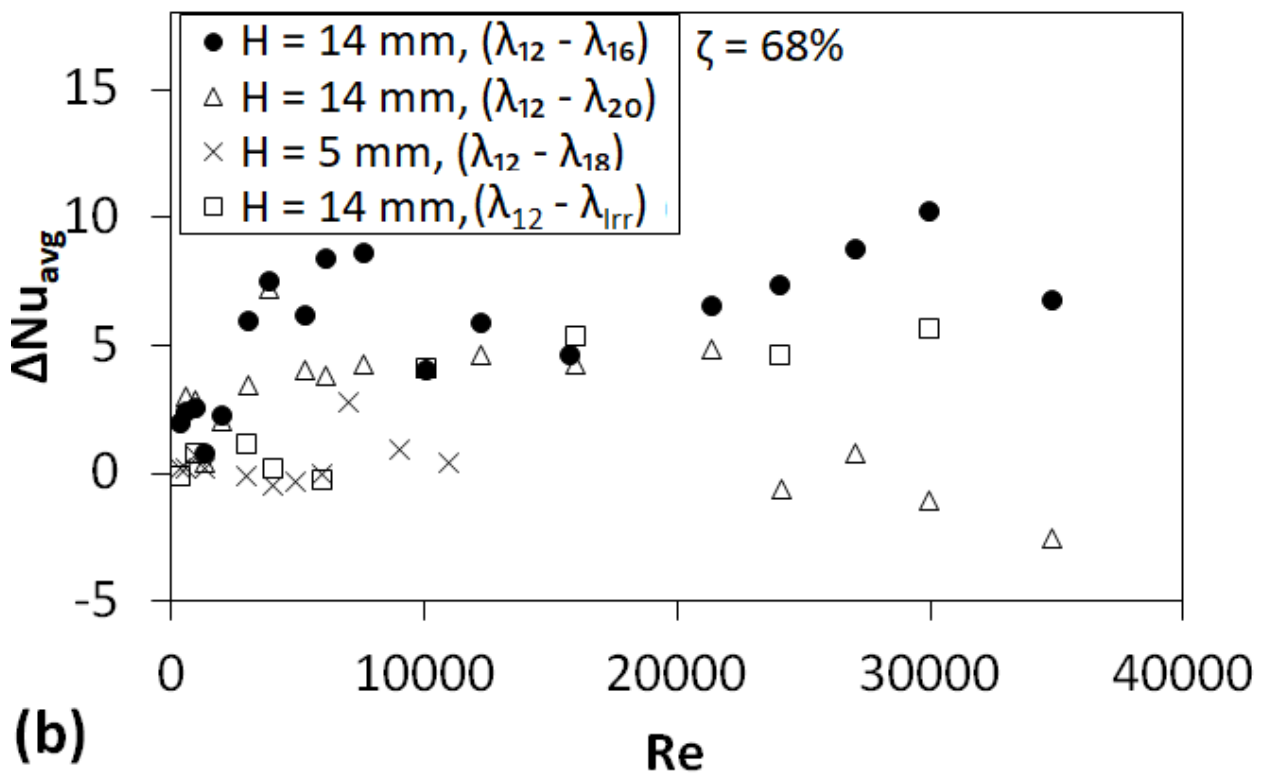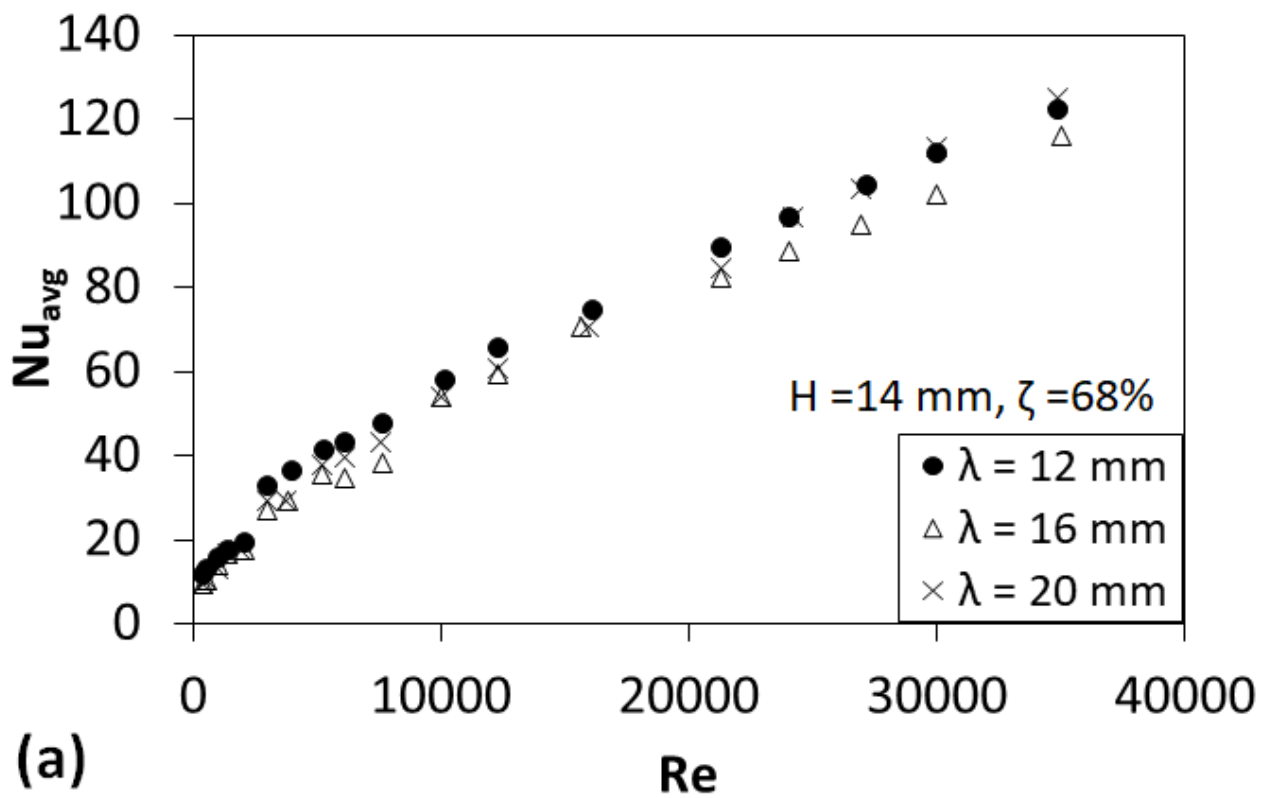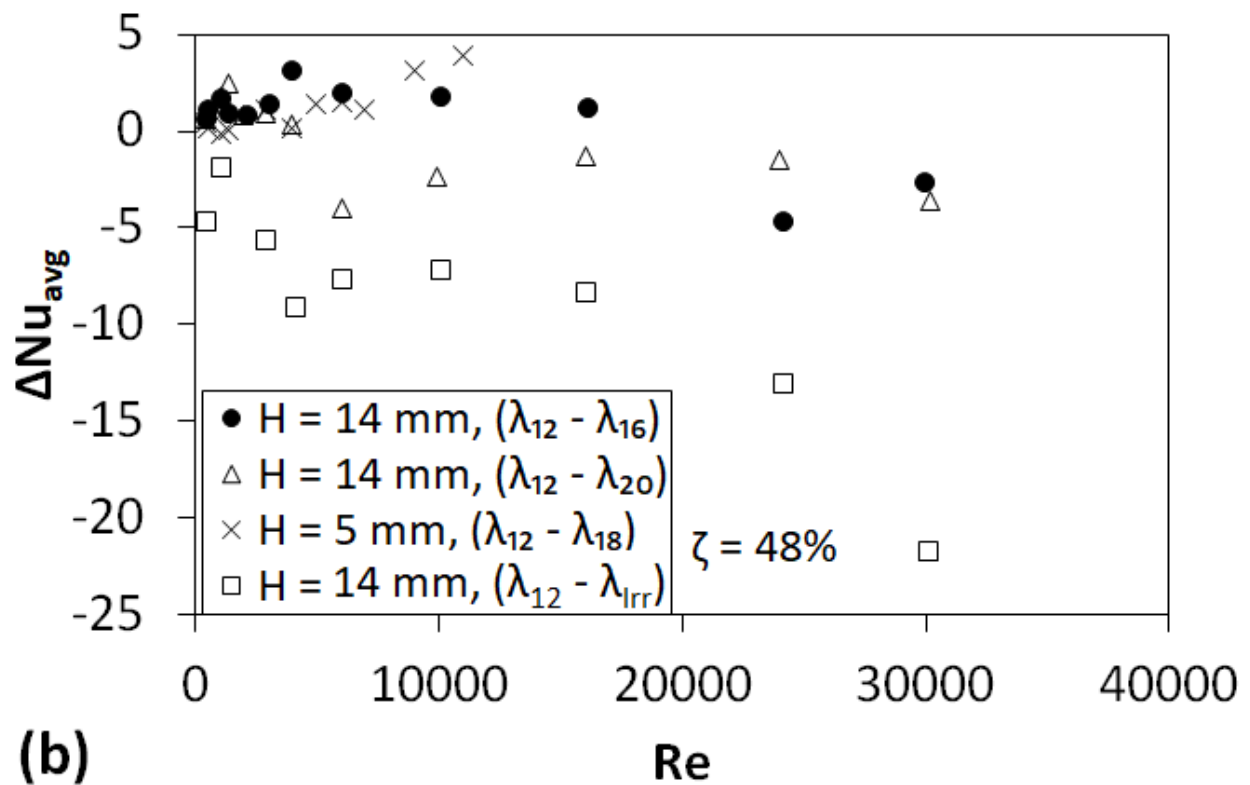
Figure 9: Average Nusselt number (Nu_{avg}) versus Reynolds number (Re) with two-wall heating for ζ = 68% inserts: (a) H = 14 mm, λ = (12 mm, 16 mm, 20 mm), and (b) difference in Nusselt number (ΔNu_{avg}) as λ increases from 12 mm.

TSEA-19-1371   Mahmood

Figure 10: Average Nusselt number (Nu_{avg}) versus Reynolds number (Re) with two-wall heating for $\zeta = 48\%$ inserts: (a) H = 14 mm, $\lambda = (12$ mm, 16 mm, 20 mm), and (b) difference in Nusselt number (ΔNu_{avg}) as λ increases from 12 mm.
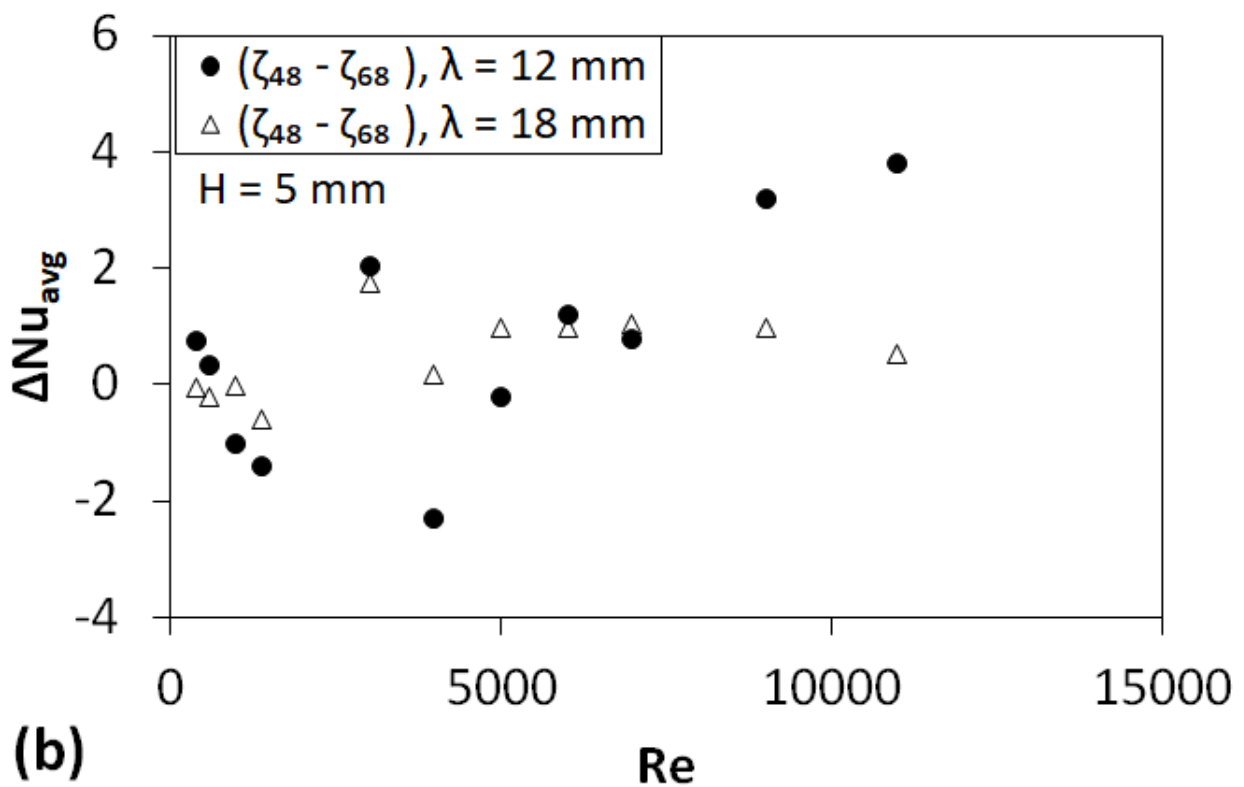
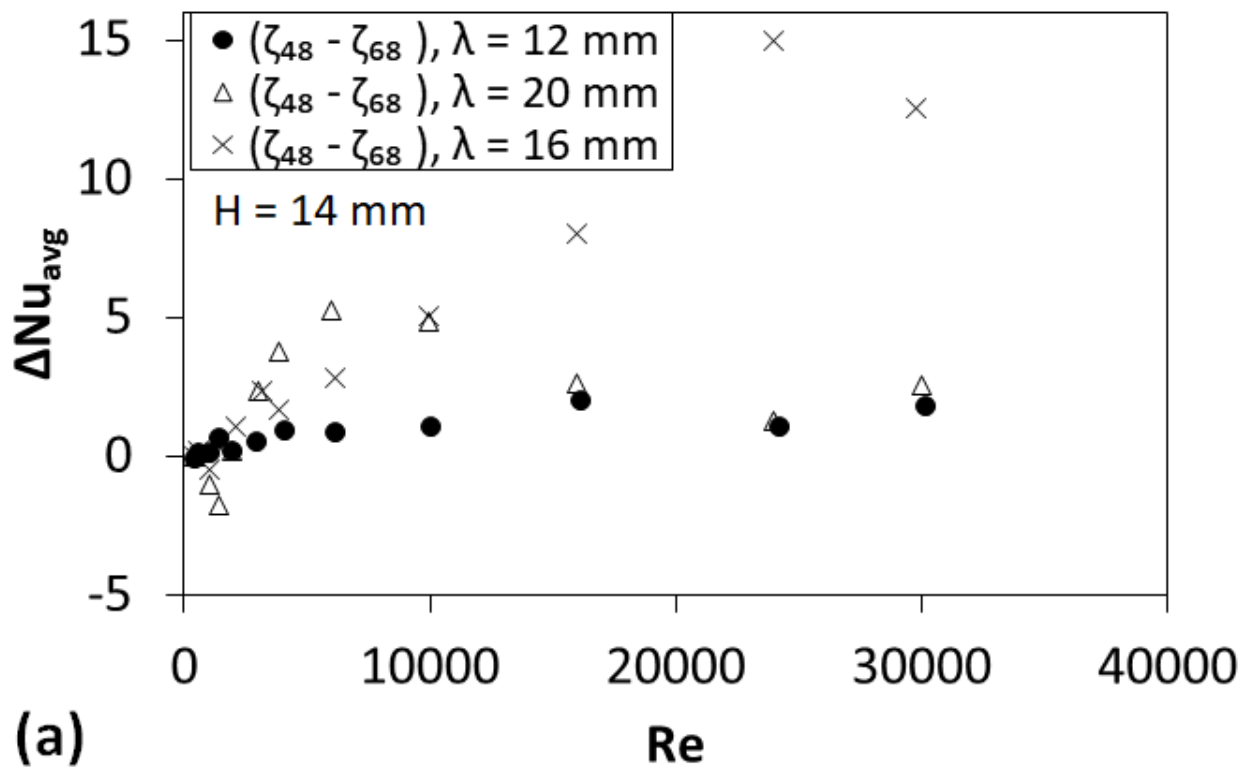TSEA-19-1371   Mahmood
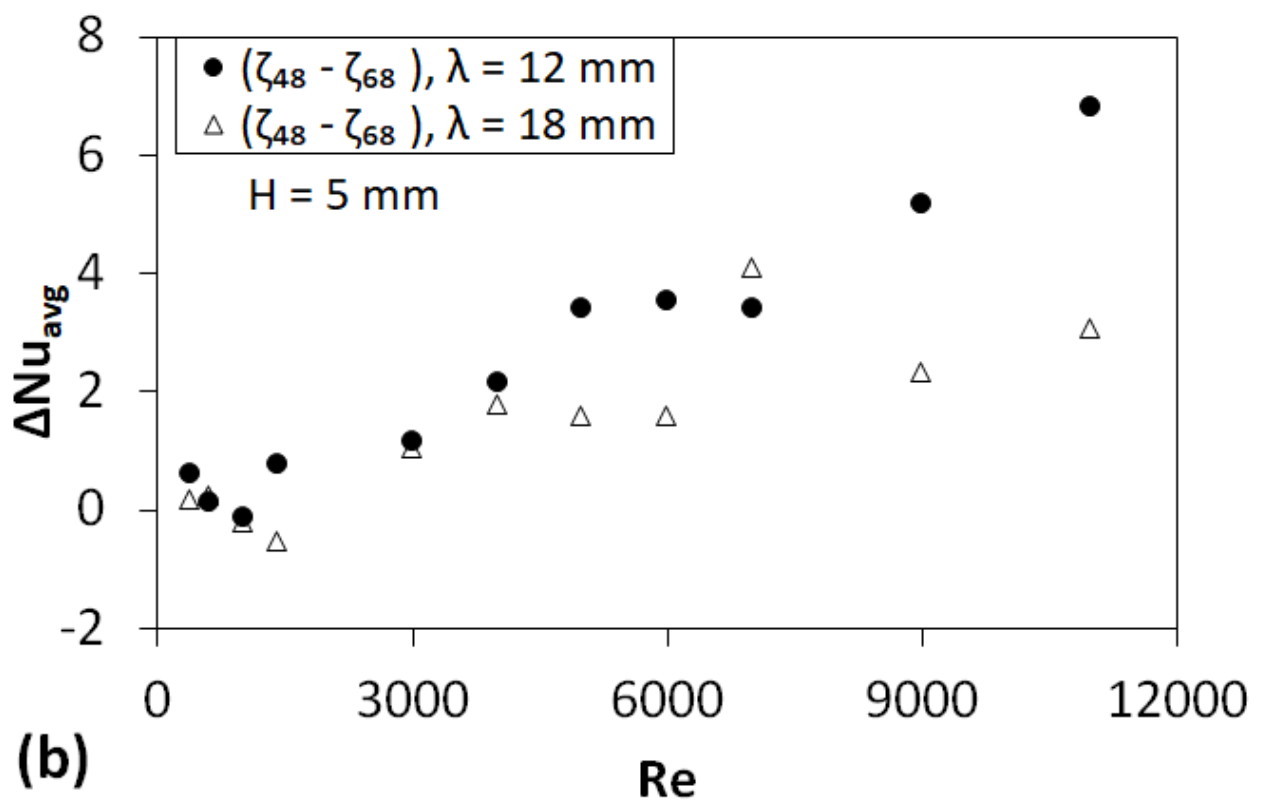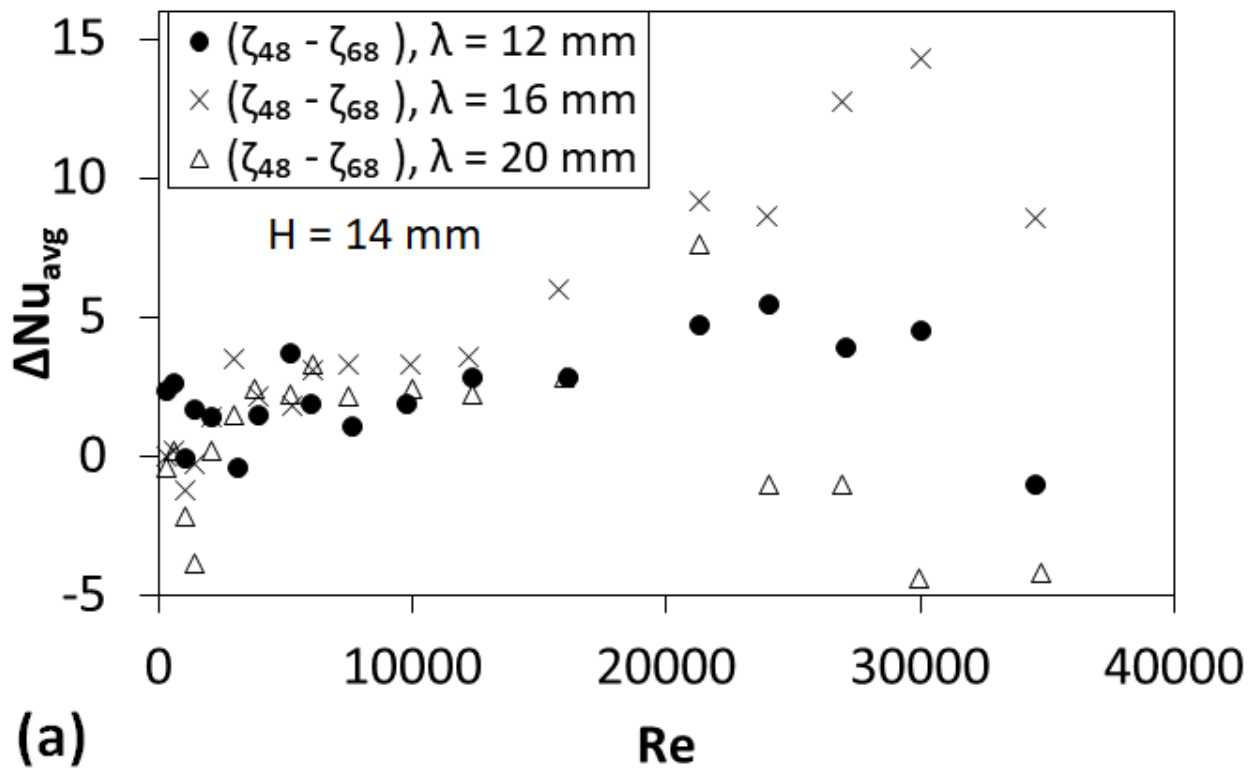
Figure 11: Decrease in average ΔNu_{avg} versus Re with two-wall heating as porosity, ξ increases from 48% to 68%: (a) H =14 mm, λ = (12 mm, 16 mm, 20 mm), and (b) H = 5 mm, λ = (12 mm, 18 mm).
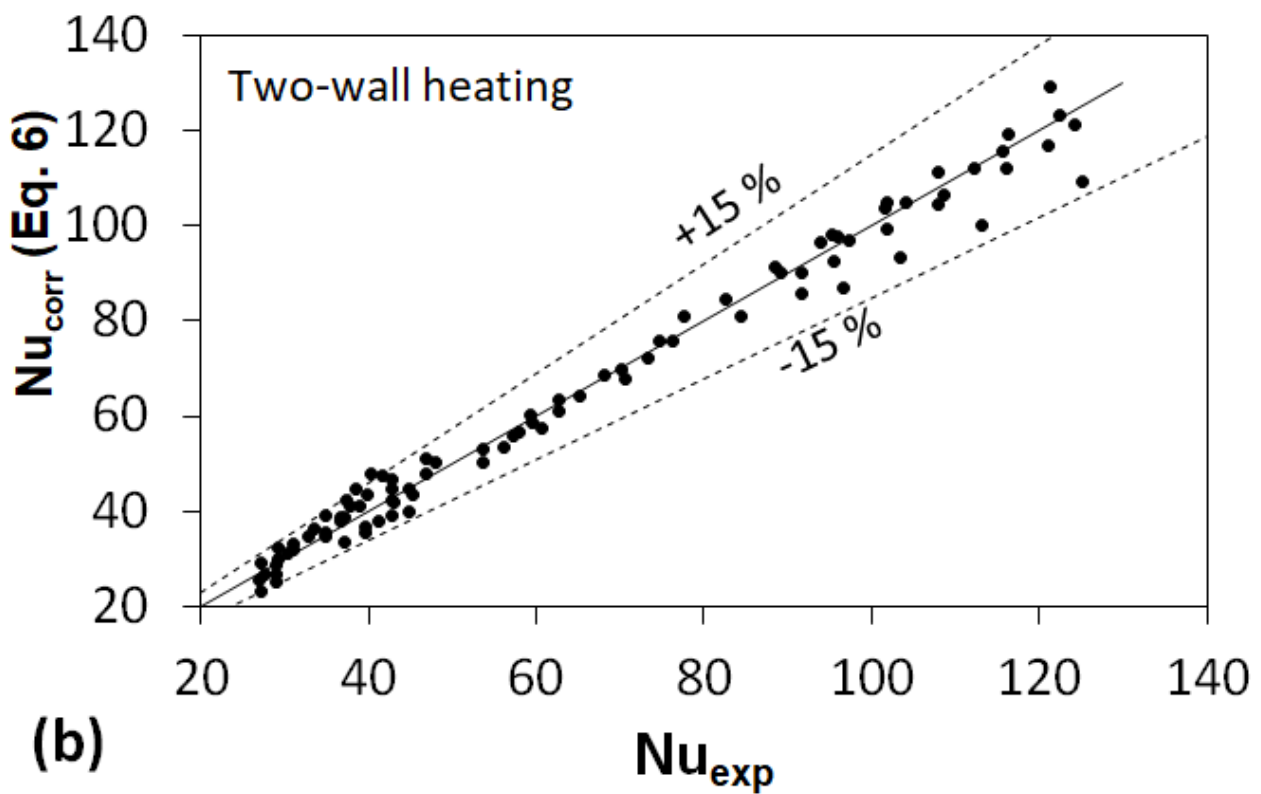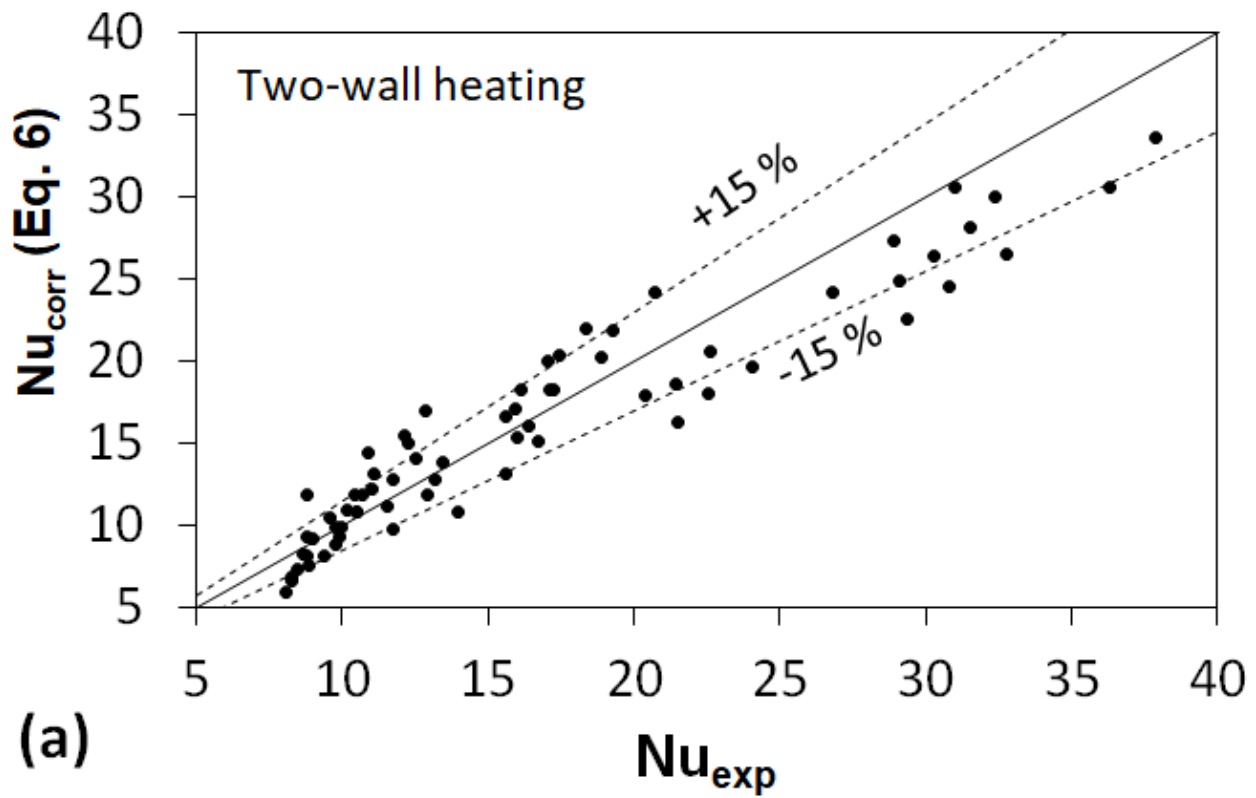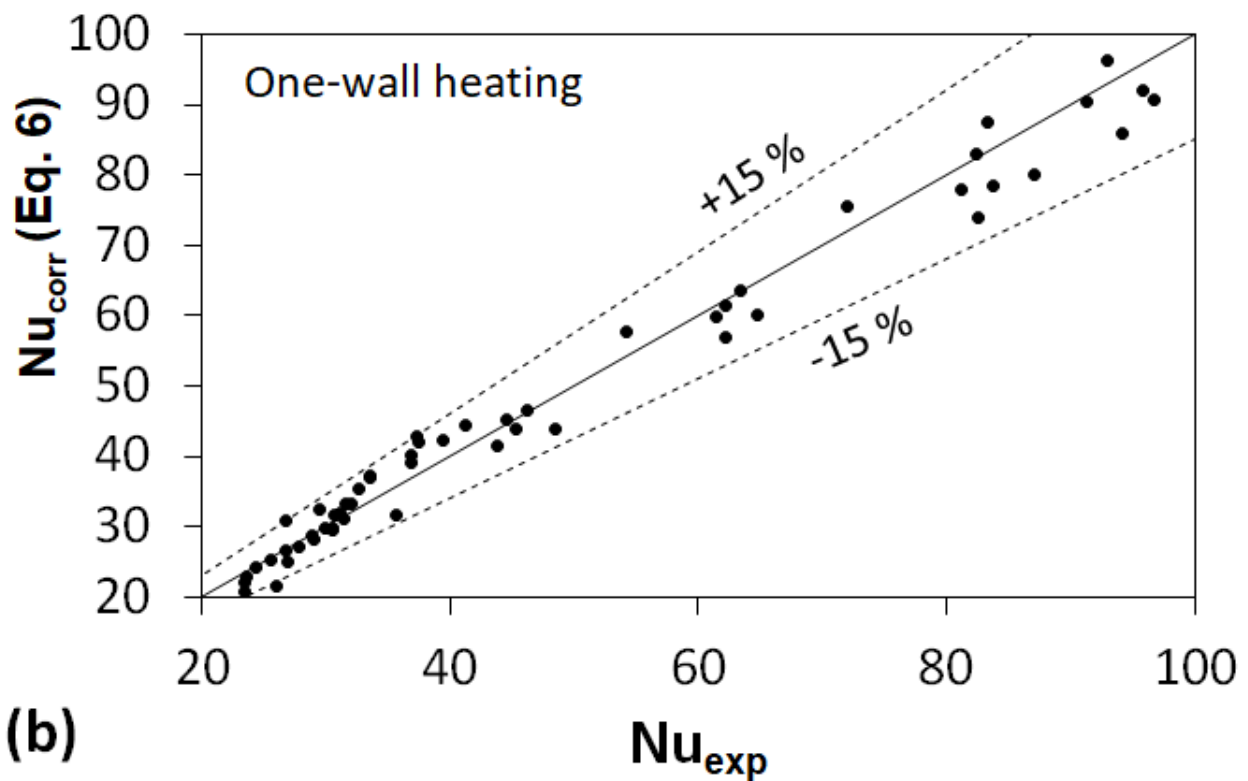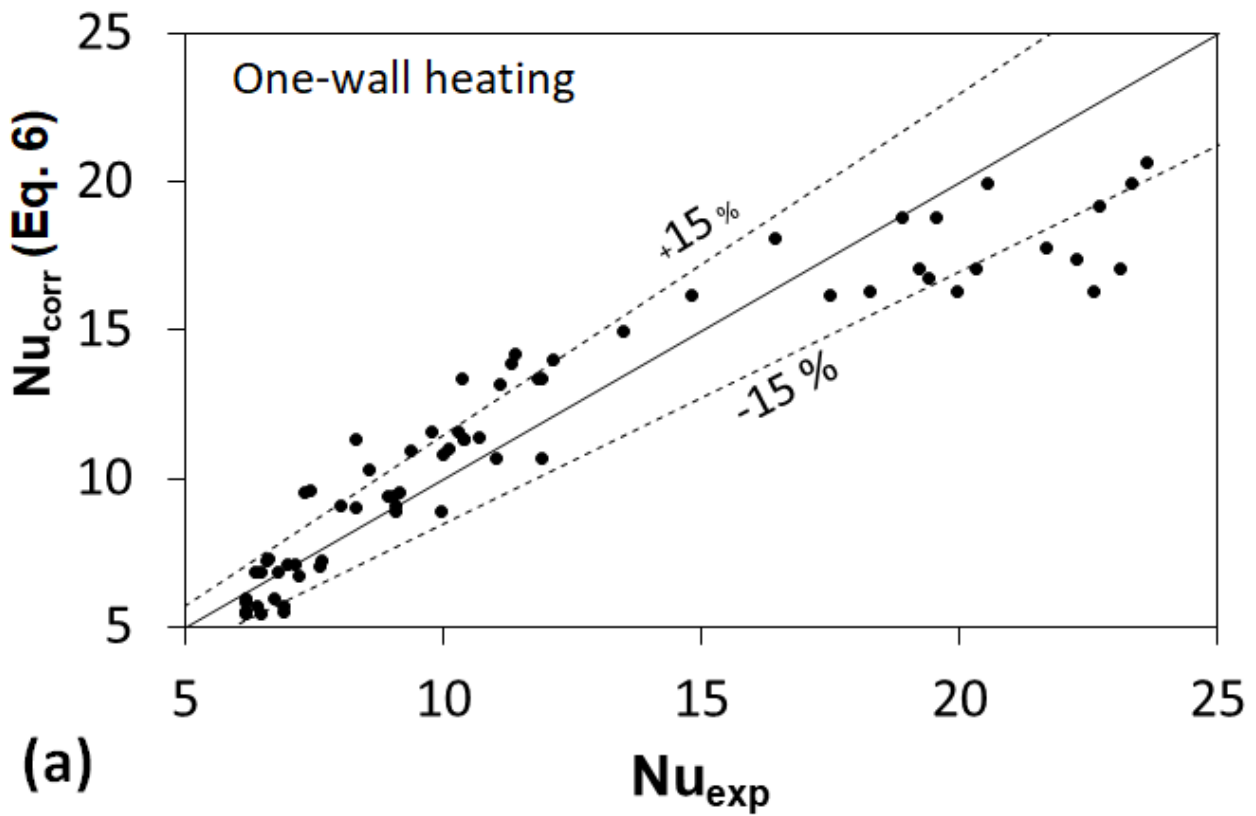
Figure 12: Comparisons of average Nusselt numbers from correlation, Nu_{corr} of Eq. (6) with those from experiments, Nu_{exp} with two-wall heating for: (a) $400 < Re < 4000$, and (b) $4000 < Re < 35000$ (inclusive of all ζ, λ, H, Re).
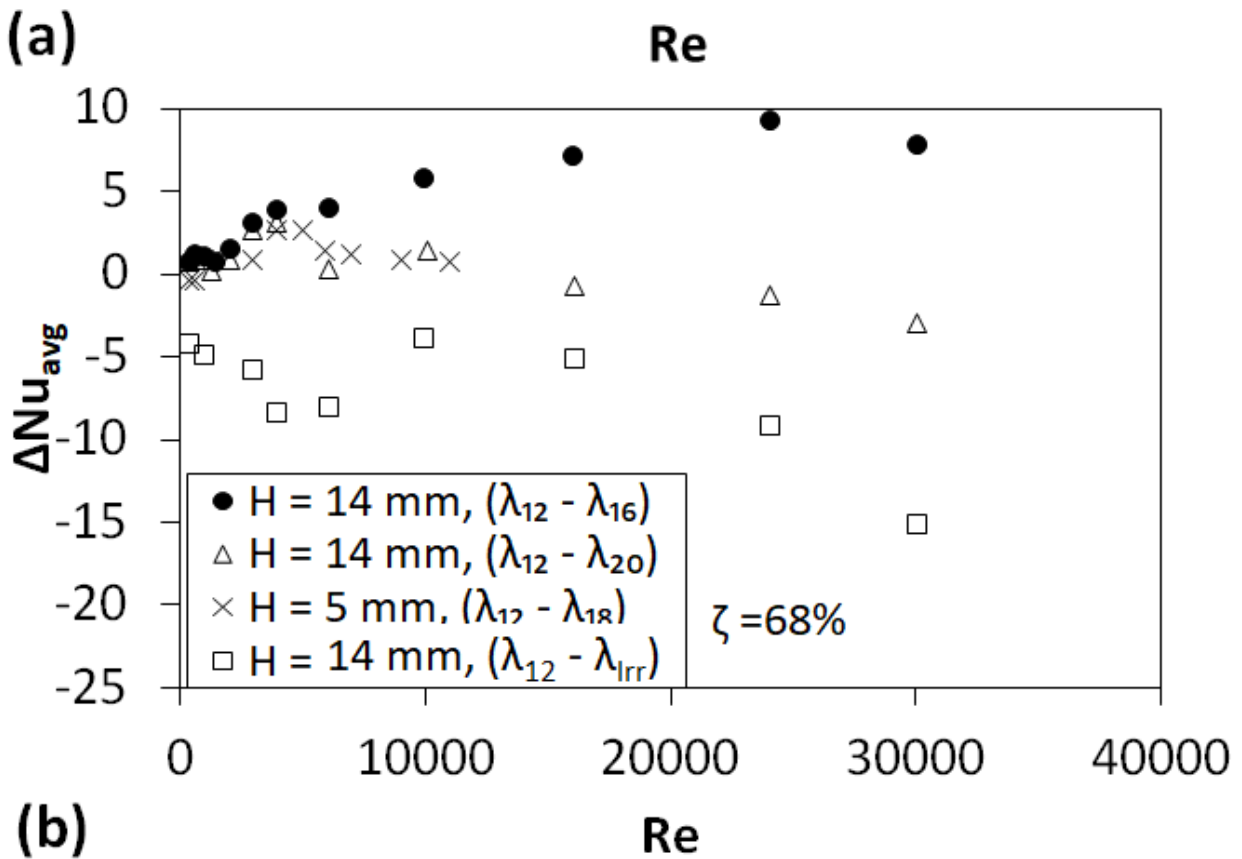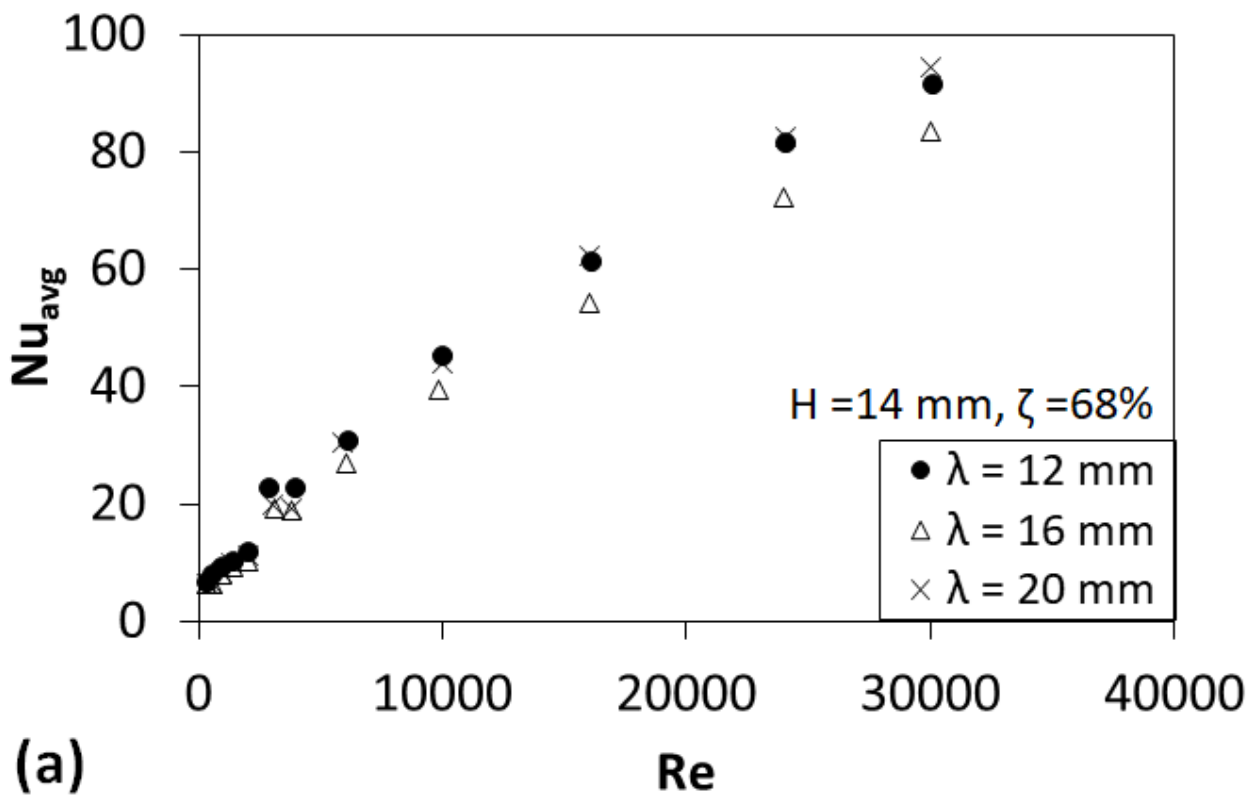
Figure 13: Average Nusselt number (Nu$_{avg}$) versus Reynolds number (Re) with one-wall heating for

$\zeta = 68\%$ inserts: (a) H = 14 mm, λ = (12 mm, 16 mm, 20 mm), and (b) difference in Nusselt number

(ΔNu$_{avg}$) as λ increases from 12 mm.

Figure 14: Average Nusselt number (Nu_{avg}) versus Reynolds number (Re) with one-wall heating for

$\zeta = 48\%$ inserts: (a) H = 14 mm, λ = (12 mm, 16 mm, 20 mm), and (b) difference in Nusselt number

(ΔNu_{avg}) as λ increases from 12 mm.

TSEA-19-1371   Mahmood

Figure 15: Decrease in average ΔNu_{avg} versus Re with one-wall heating as porosity, ξ increases from 48% to 68%: (a) H =14 mm, λ = (12 mm, 16 mm, 20 mm), and (b) H = 5 mm, λ = (12 mm, 18 mm).

Figure 16: Comparisons of average Nusselt number from correlation with one-wall heating, Nu_{corr} of Eq. (6) with those from experiments, Nu_{exp} for: (a) $400 < Re < 4000$, and (b) $4000 < Re < 35000$ (inclusive of all ζ, λ, H, Re). Constants in Eq. (6) are different from those for two-wall heating.
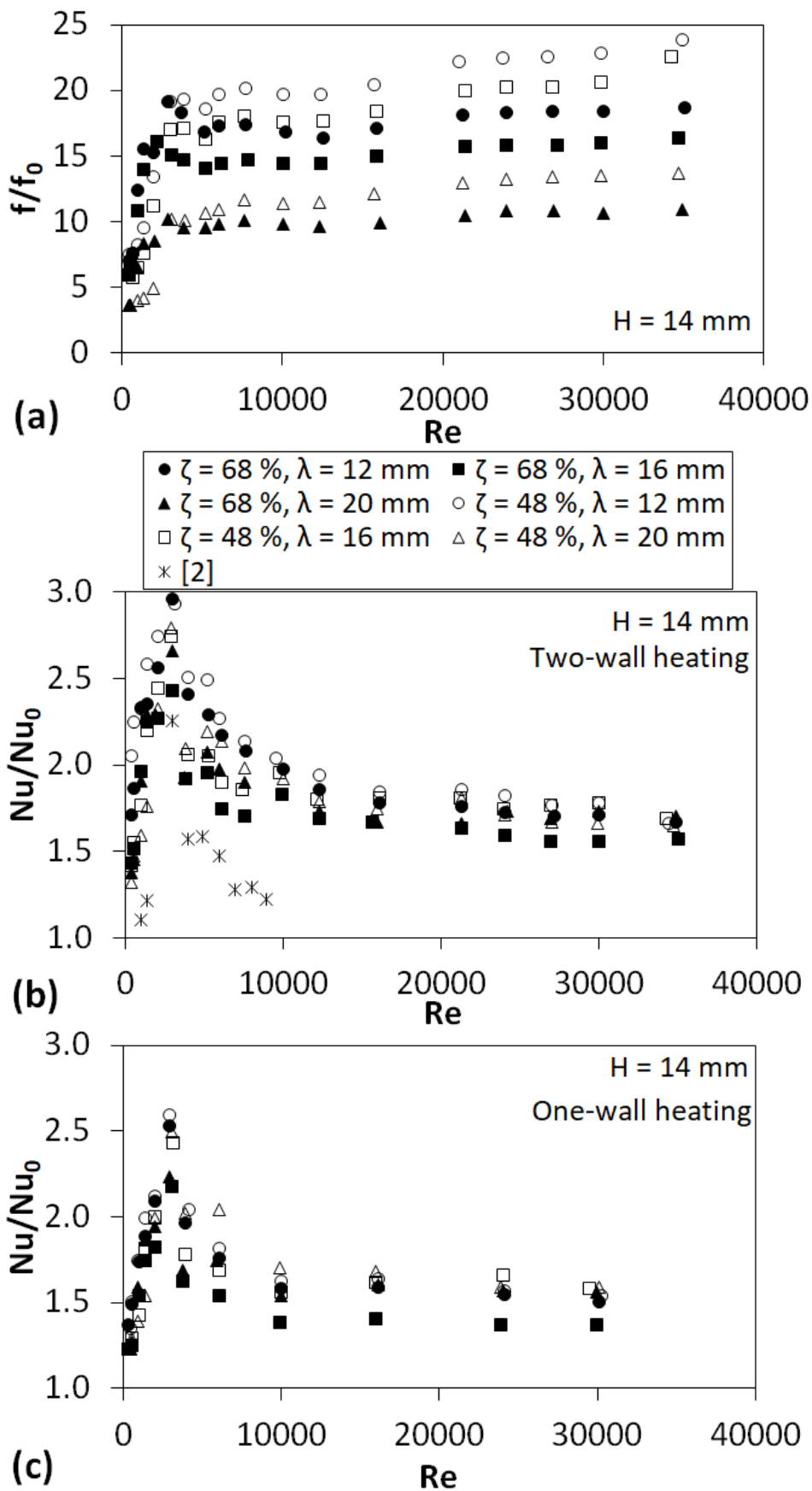
Figure 17: Performance of f and Nu_{avg} vs. Re relative to smooth channel for the H = 14 mm inserts:

(a) f/f_0, (b) Nu/Nu_0 with two-wall heating, and (c) Nu/Nu_0 with one-wall heating.
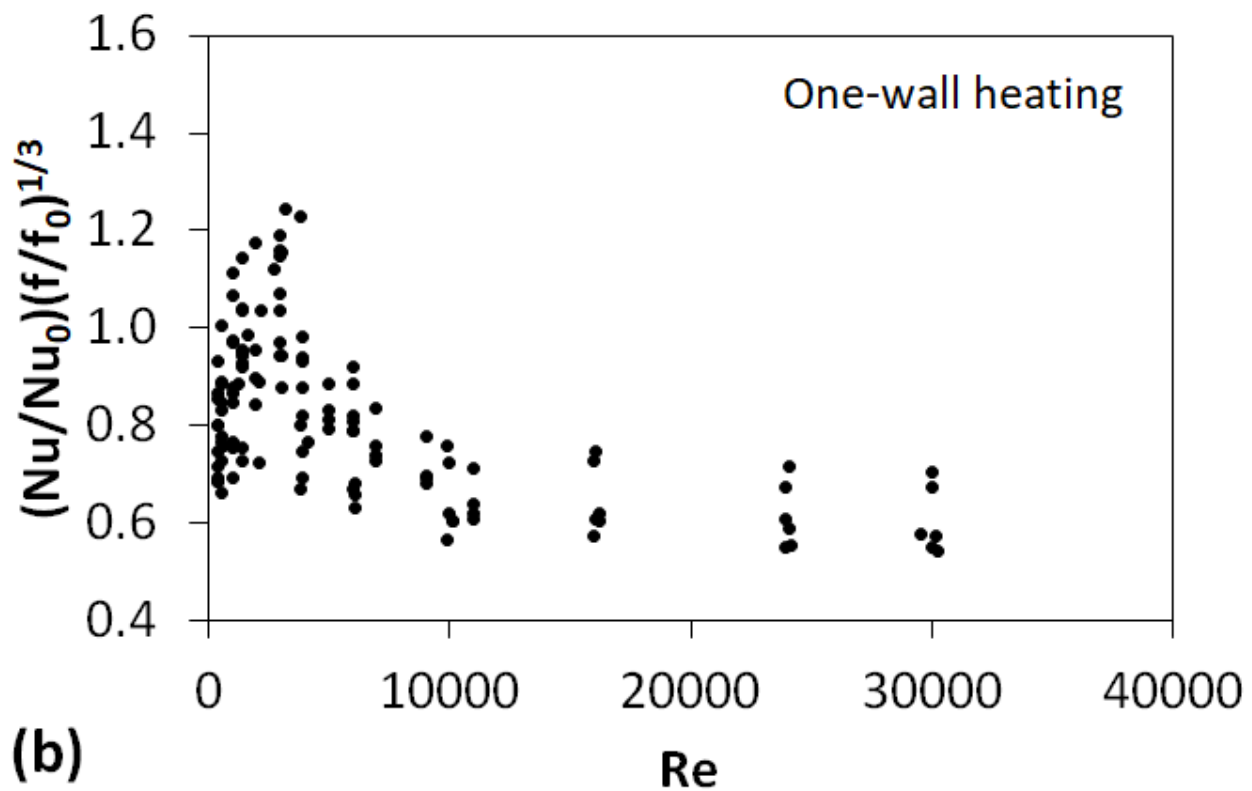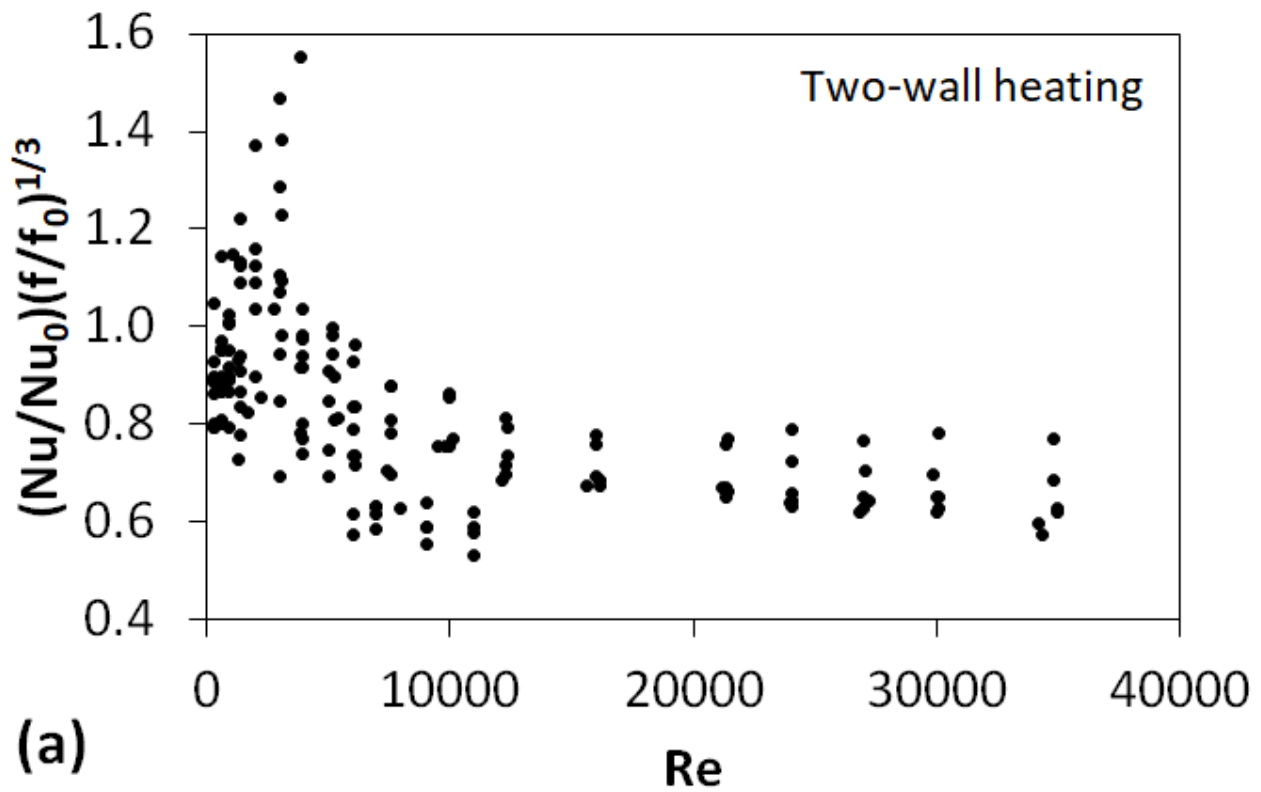
Figure 18: Performance factor (PF) as Re increases (inclusive of all ζ, λ, H) for: (a) two-wall heating and (b) one-wall heating.
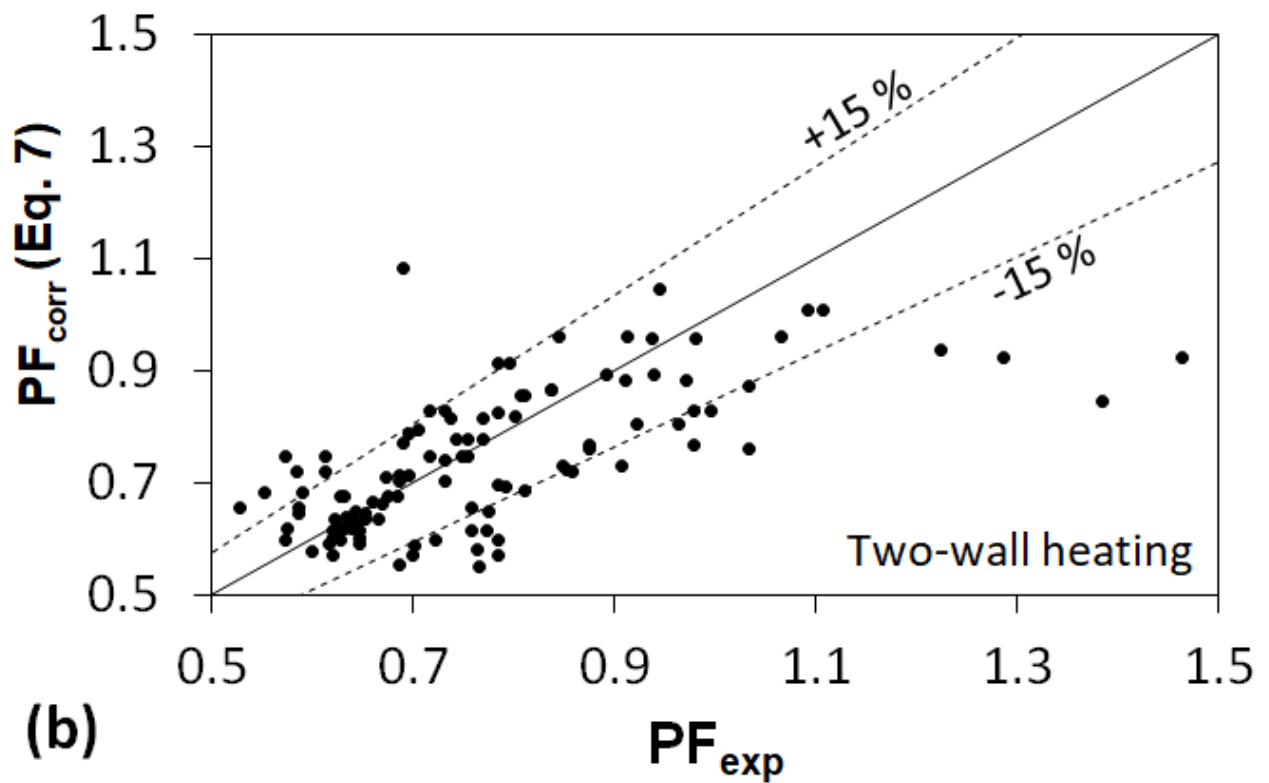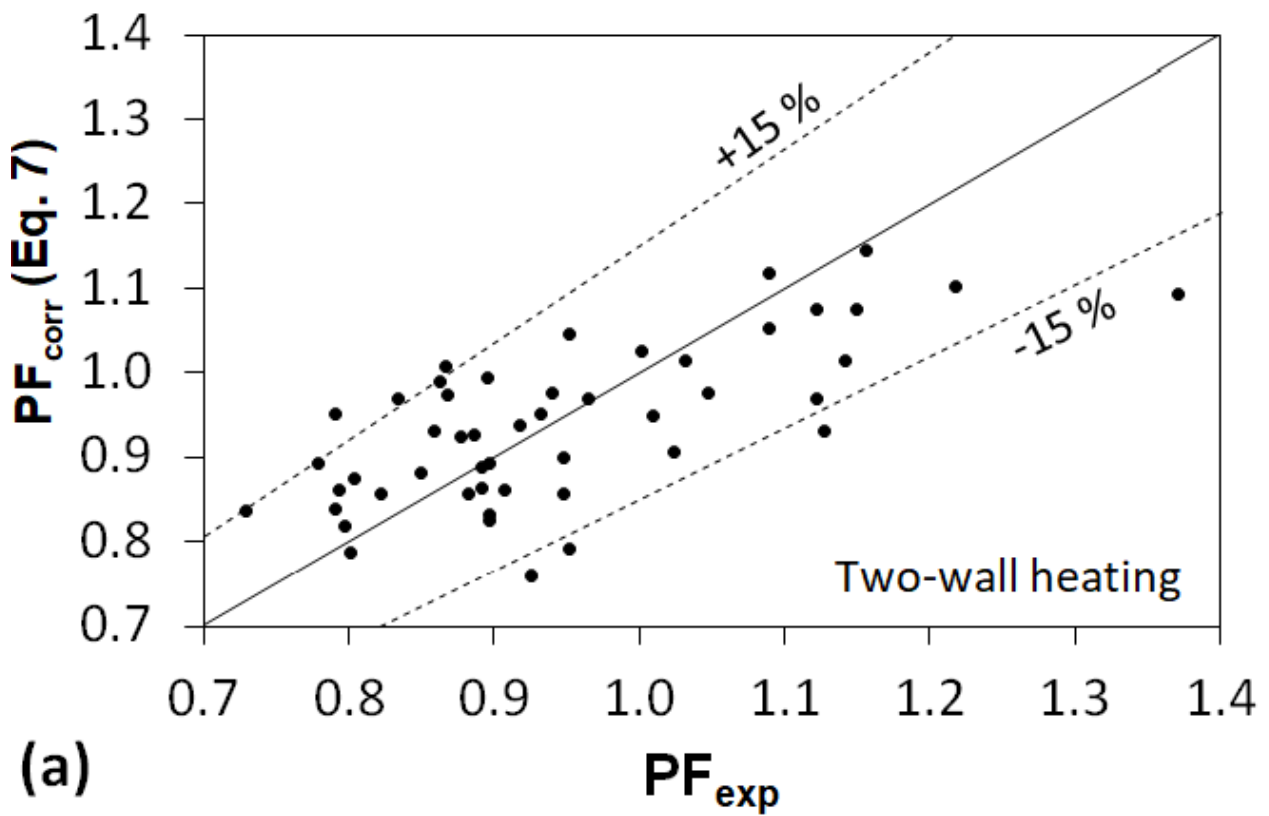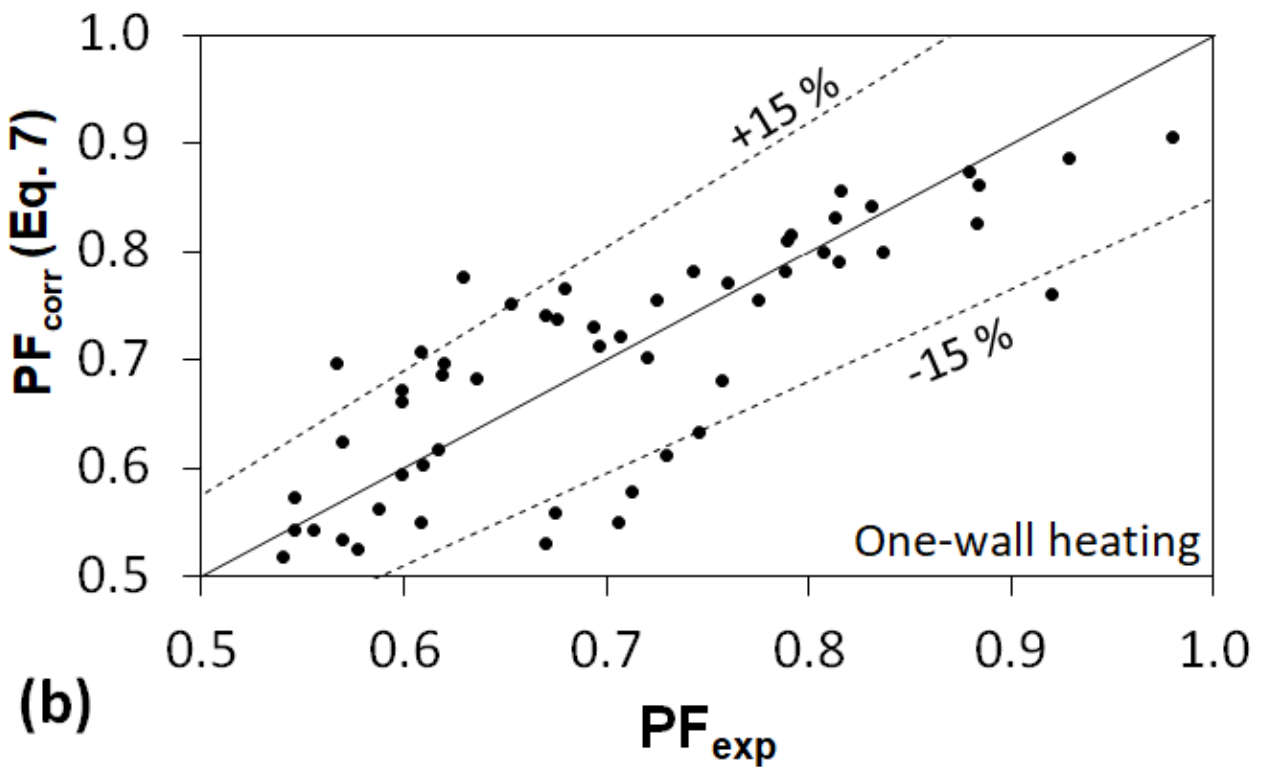
Figure 19: Comparisons of performance factor from correlation with two-wall heating, PF_{corr} of Eq. (7) with those from experiments, PF_{exp} for: (a) $400 < Re < 2100$, and (b) $2100 < Re < 35000$ (inclusive of all ζ, λ, H, Re).
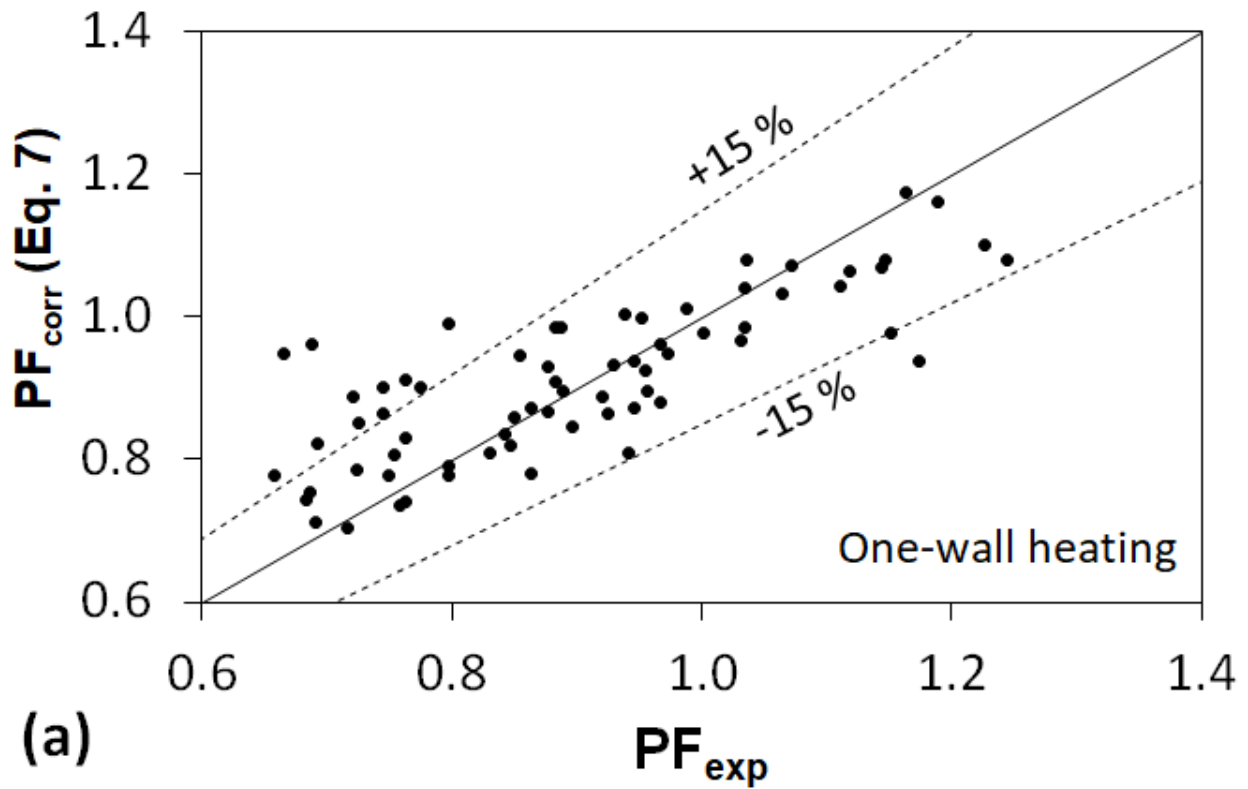
Figure 20: Comparisons of performance factor from correlation with one-wall heating, PF_{corr} of Eq. (7) with those from experiments, PF_{exp} for: (a) $400 < Re < 4000$, and (b) $4000 < Re < 30000$ (inclusive of all ζ, λ, H, Re). Constants in Eq. (7) are different from those for two-wall heating.

TSEA-19-1371   Mahmood